The Orinoco Low-Level Jet: An Investigation of its Mechanisms of Formation Using the WRF Model

Giovanni Jiménez-Sánchez[1,2], Paul M. Markowski[1], George S. Young[1], and David J. Stensrud[1]

[1]Department of Meteorology and Atmospheric Science, The Pennsylvania State University, University Park, Pennsylvania.

[2]Fuerza Aérea Colombiana, Bogotá, D.C., Colombia.

Corresponding author: Dr. Giovanni Jiménez-Sánchez (jorge.jimenez@fac.mil.co)

Key Points:

- The Orinoco low-level jet is the result of four phenomena acting together to accelerate the wind over the valley of the Orinoco River basin.
- Opposite to what happens in higher latitudes, the role of the diurnal variation of turbulent diffusivity in the Orinoco low-level jet acceleration is secondary.
- Low-level jets near the equator may originate from processes other than the inertial oscillation and topographic thermal forcing.

Abstract

The Orinoco low-level jet (OLLJ) is characterized using finer horizontal, vertical, and temporal resolution than possible in previous studies via dynamical downscaling. The investigation relies on a 5-month-long simulation (November 2013-March 2014) performed with the WRF model, with initial and boundary conditions provided by the GFS analysis. Dynamical downscaling is demonstrated to be an effective method not only to better resolve the horizontal and vertical characteristics of the Orinoco low-level jet but also to determine the mechanisms leading to its formation.

The OLLJ is a single stream tube over Colombia and Venezuela with wind speeds greater than 8 m s^{-1}, and four distinctive cores of higher wind speeds varying in height under the influence of sloping terrain. It is an austral summer phenomenon that exhibits its seasonal maximum wind speed and largest spatial extent (2100 km × 450 km) in January. The maxima diurnal mean wind speeds (13–17 m s^{-1}) at each core location occur at different times during the night (2300–0900 LST).

The momentum balance analysis in a natural coordinate system reveals that the OLLJ results from four phenomena acting together to accelerate the wind: a sea-breeze penetration, katabatic flow, three expansion fans, and diurnal variation of turbulent diffusivity. The latter, in contrast to the heavily studied nocturnal low-level jet in the U.S. Great Plains region, plays a secondary role in OLLJ acceleration. These results imply that LLJs near the equator may originate from processes other than the inertial oscillation and topographic thermal forcing.

1 Introduction

The occurrence of nocturnal low-level wind speed maxima—i.e., nocturnal low-level jets (LLJs)—is usually explained through the inertial oscillation and topographic thermal forcing mechanisms. The inertial oscillation mechanism, originally proposed by Blackadar (1957) and subsequently modified by Van de Wiel et al. (2010), attributes the acceleration of the wind to the imbalance of forces occurring at sunset once turbulent mixing ceases, which effectively leads to a vanishing of the drag force in the residual layer above the shallow stable nocturnal boundary layer (Stull, 2015a). Without this frictional force, the horizontal wind accelerates, which in turn increases the Coriolis acceleration, ultimately causing the wind to oscillate about its geostrophic velocity. The velocity becomes most supergeostrophic when the ageostrophic wind component (its magnitude increases with an increasing frictional force acting on the upper-boundary-layer wind during the daytime period) rotates to an orientation aligned with the geostrophic velocity. Although the rotation rate of the ageostrophic velocity increases with latitude, the LLJ typically reaches its maximum wind speed 4–6 hours after sunset.

The topographic thermal forcing mechanism, introduced by Holton (1967), accounts for the effect that the diurnal oscillation of the horizontal temperature gradient over sloping terrain has on the direction of the thermal wind. At night, when the air adjacent to the slope cools more than the surrounding air at the same level, the thermal wind reverses its daytime direction, implying a poleward acceleration of the wind above the slope.

Both mechanisms may act together to produce an enhanced wind speed maximum, as is the case in the Great Plains LLJ (Bonner & Paegle, 1970; Du & Rotunno, 2014; Shapiro et al., 2016), or they can independently generate an LLJ (Du & Rotunno, 2014; Fedorovich et al., 2017; Stensrud, 1996); however, when only one of the mechanisms is considered, the LLJ is usually

less predictable in time, and/or weaker than observed (Du & Rotunno, 2014; Shapiro et al., 2016). Recently, Parish (2017) stated that the inertial oscillation is the most important forcing in the Great Plains LLJ generation, giving only marginal relevance to the sloping-terrain diurnal heating variation. The development of a strong background pressure-gradient force (PGF), via long-term heating, is proposed to be of greater importance than the daily heating oscillations.

Although extensive research has been done on LLJs in the U.S. Great Plains (e.g., Blackadar, 1957; Bonner, 1963, 1968; Bonner & Paegle, 1970; Du et al., 2014; Holton, 1967; Krishnamurthy et al., 2015; Parish, 2017; Shapiro et al., 2016; Song et al., 2005; Squitieri, 2014; Weaver & Nigam, 2008; Wexler, 1961; Whiteman et al., 1997; Wu & Raman, 1993), and in other parts of the world as well (e.g., Amador, 2008; Balmez & Ştefan, 2014; G. T.-J. Chen & Hsu, 1997; R. Chen & Tomassini, 2015; Cook & Vizy, 2010; Doyle & Warner, 1993; Du et al., 2014; Du, Chen, et al., 2015; Du, Rotunno, et al., 2015; Findlater, 1969; Giannakopoulou & Toumi, 2012; Hart, 1977; He et al., 2016; Hidalgo et al., 2015; Juliano et al., 2017; Liu et al., 2000; Maldonado et al., 2016, 2017; Marengo et al., 2004; Muñoz et al., 2008; Do Nascimento et al., 2016; Nicholson, 2016; Patricola & Chang, 2017; G Poveda & Mesa, 1999; Germán Poveda et al., 2014; Germán Poveda & Mesa, 2000; Prabha et al., 2011; Rojas, 2008; O. Rueda & Poveda, 2006; Silva et al., 2009; Soares et al., 2014; Vera et al., 2006; Virji, 1981; Wang et al., 2008; Wei et al., 2013; Whyte et al., 2008; Zhao et al., 2003), just a few authors have investigated the low-level wind maximum occurring during the Austral summer in the savannas of the Orinoco River basin. Hereafter, this phenomenon is referred to as the Orinoco low-level jet (OLLJ).

The OLLJ could have been noticed in the examination of the lower tropospheric winds from satellite images performed by Virji (1981), or in the reanalysis data over South America examined by Montoya et al. (2001), but the existence of a larger-scale wind phenomenon—the South American low-level jet (Montini et al., 2019)—prevented its detection until recently. The identification and characterization of the OLLJ was subsequently achieved using mesoscale simulations (Rife et al., 2010; Vernekar et al., 2003) and a combination of pilot balloons, radiosondes, surface data, and more recent versions of reanalysis (e.g., Douglas et al., 2005; Labar et al., 2005; C. Rueda, 2015; Torrealba & Amador, 2010). However, the physical mechanisms of its formation have not yet been established.

Vernekar et al. (2003), Labar et al. (2005), and Rueda (2015) have hypothesized that the OLLJ formation is the result of the PGF between the North Atlantic subtropical high and the low pressure over Amazonia, when the Intertropical Convergence Zone (ITCZ)—also called the Near-Equatorial Trough (NET)—migrates southward during austral summer (Fig. 1a). As a result, the northeasterly trade winds strengthen while undergoing topographic channeling between the Coastal Cordillera and the Guiana Highlands. Diurnal heating and cooling of the basin, as well as differential heating between the mountains and the plains, the land and the ocean, produce changes in the vertical mixing of the air's horizontal momentum, modifying the OLLJ diurnal behavior. The studies performed by Rueda (2015) using ERA-Interim (1983–2013) showed that the OLLJ is only present from November to March, whereas the rest of the year the northward migration of the ITCZ (Fig. 1b) weakens the LLJ and introduces southeasterly trade winds into the basin.

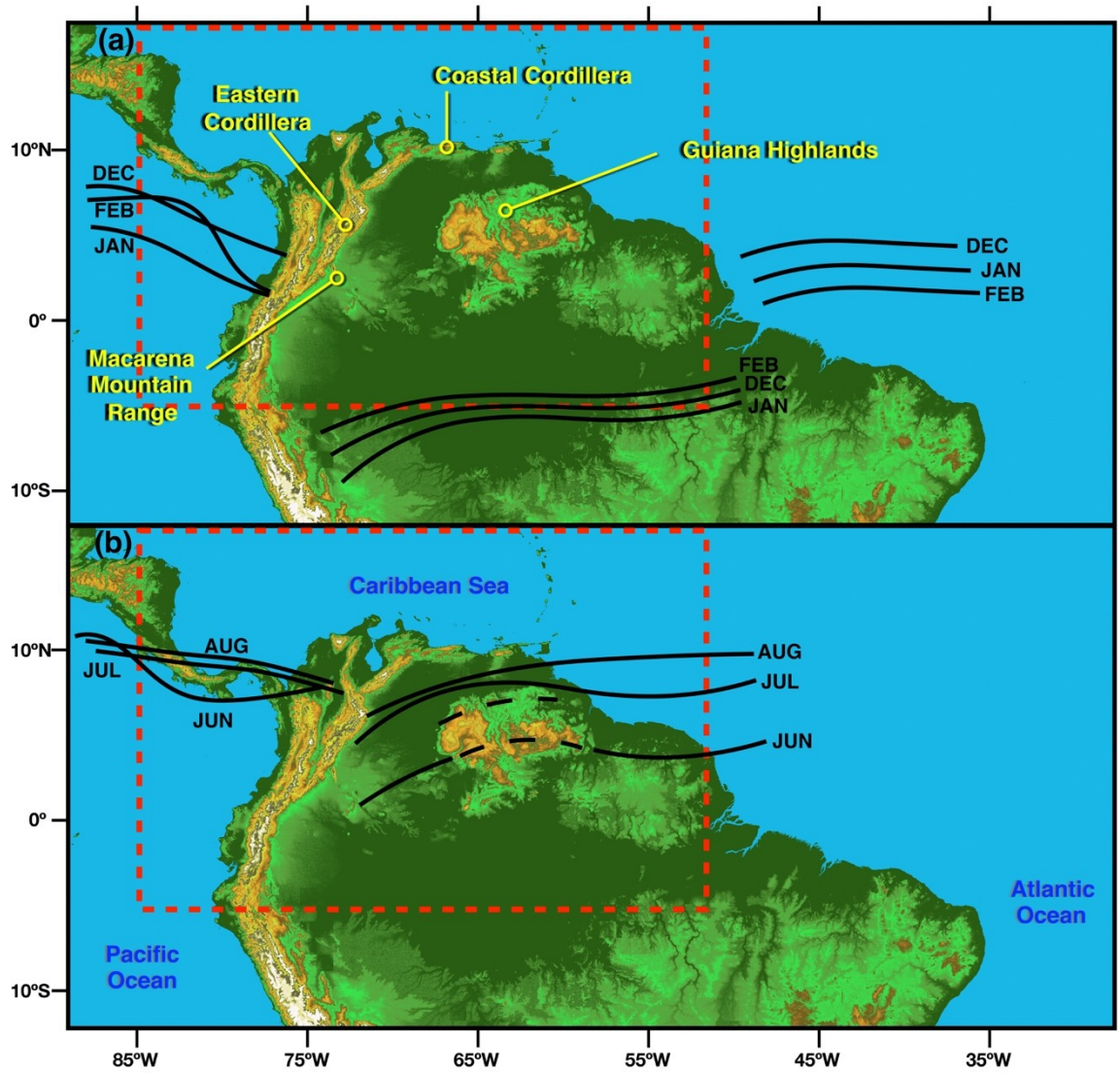

Figure 1. Map of northern South America displaying the mean Near-Equatorial Trough (NET) positions (black lines) during the (a) austral summer and (b) austral winter. Black dashed lines show two possible mean June positions. The mountainous terrain in the northern part of the continent disrupts the NET and makes the mean position variable [Adapted from Fig. 2-5 in Gilford et al. (1992)]. The limits of the WRF-ARW domain are shown in red.

The purpose of this work is to investigate the physical mechanisms of formation of the OLLJ by performing a dynamical downscaling of the large-scale atmospheric conditions provided by the Global Forecast System (GFS) analysis data, and a momentum balance evaluation similar to that used by Doyle & Warner (1993), Rife et al. (2010), Du et al. (2014); Du, Chen, et al. (2015); Du, Rotunno, et al. (2015); and He et al. (2016). The dynamical downscaling provides greater detail than in previous studies about the OLLJ structure and evolution (Jiménez-Sánchez et al., 2019), and the momentum balance analysis is used to determine the forcings for the wind acceleration responsible for the OLLJ.

The findings suggest that the OLLJ is the result of several mesoscale mechanisms acting together to accelerate the wind, and because of its proximity to the equator, existing theories explaining the behavior of higher-latitude LLJs apply only partially to the OLLJ formation.

The next section describes the model configuration and momentum-balance analysis method. Section 3 analyzes the results and discusses the mechanisms of OLLJ formation. Finally, a summary and conclusions are presented.

2 Data and methods

To characterize the behavior of the OLLJ and the complex topography surrounding the Orinoco River basin, the nonhydrostatic version 3.4.1 of the Advanced Research-WRF model (WRF-ARW; Skamarock & Klemp, 2008) is used to perform a dynamical downscaling of the large-scale atmospheric conditions. This modeling technique enables finer spatial and temporal resolutions than in previous studies. Figure 1 shows the limits of the model domain, which is centered at 7ºN and 68.5ºW, and the main topographic features along the OLLJ corridor.

The WRF-ARW physical parameterization schemes/models, the initial and boundary conditions, as well as the spatial and temporal resolutions are the same described in Jiménez-Sánchez et al.(2019), where the period of study (November 2013–March 2014) provides the opportunity to analyze the OLLJ isolating the wind variability produced by El Niño-Southern Oscillation (ENSO). The model simulations were validated using NCEP FNL Operational Global Analysis and GFS Analysis files, which evidenced good agreement with the model (not shown).

Modifications to the WRF-ARW dynamical solver (Moisseeva & Steyn, 2014) allows the extraction of the individual tendency terms from the horizontal momentum equations so that the contribution of each forcing to the total acceleration of the wind can be assessed. After the extraction, a streamwise (s) and a crosswise (n) coordinate system is constructed applying the dot product of the wind direction unit vector and the Coriolis force direction unit vector, respectively, to each tendency term. The final momentum equations characterizing the streamwise and crosswise components of the flow are:

$$\frac{\partial V_s}{\partial t} = \frac{-\partial \Phi}{\partial s} + \left(-\mathrm{V} \cdot \nabla \mathrm{V}\right)_s - f V_n + Res \qquad (1)$$

and

$$\frac{\partial V_n}{\partial t} = \frac{-\partial \Phi}{\partial n} + \left(-\mathrm{V} \cdot \nabla \mathrm{V}\right)_n + f V_s + Res \qquad (2)$$

Eqs. (1) and (2) imply that the local acceleration of the horizontal wind (LHS), along the streamwise and crosswise axes respectively, is balanced by the sum of the horizontal PGF, horizontal advection, Coriolis force, and Residual term. The residual includes accelerations due to the vertical momentum advection, map projection, model diffusion,

and physical parameterizations, as well as errors in the calculation of the other terms. In the boundary layer, the residual is dominated by the effects of surface friction.

3 OLLJ conceptual model

As shown by Jiménez-Sánchez et al. (2019), the OLLJ is a single stream tube (2000 km long × 300 km wide × 3 km deep, approximately) over Colombia and Venezuela, with mean wind speeds greater than 8 m s^{-1}. It is an austral summer phenomenon that exhibits its seasonal maximum wind speed and largest spatial extent (2100 km × 450 km) in January (Fig. 2). The OLLJ's interaction with the surrounding topography produces four localized cores of higher wind speeds (C1–C4; Fig. 2) along its curved axis of propagation, whose mean heights above the terrain increase in the streamwise direction (~500 m, 700 m, 700 m, and 1250 m, respectively; Fig. 3).

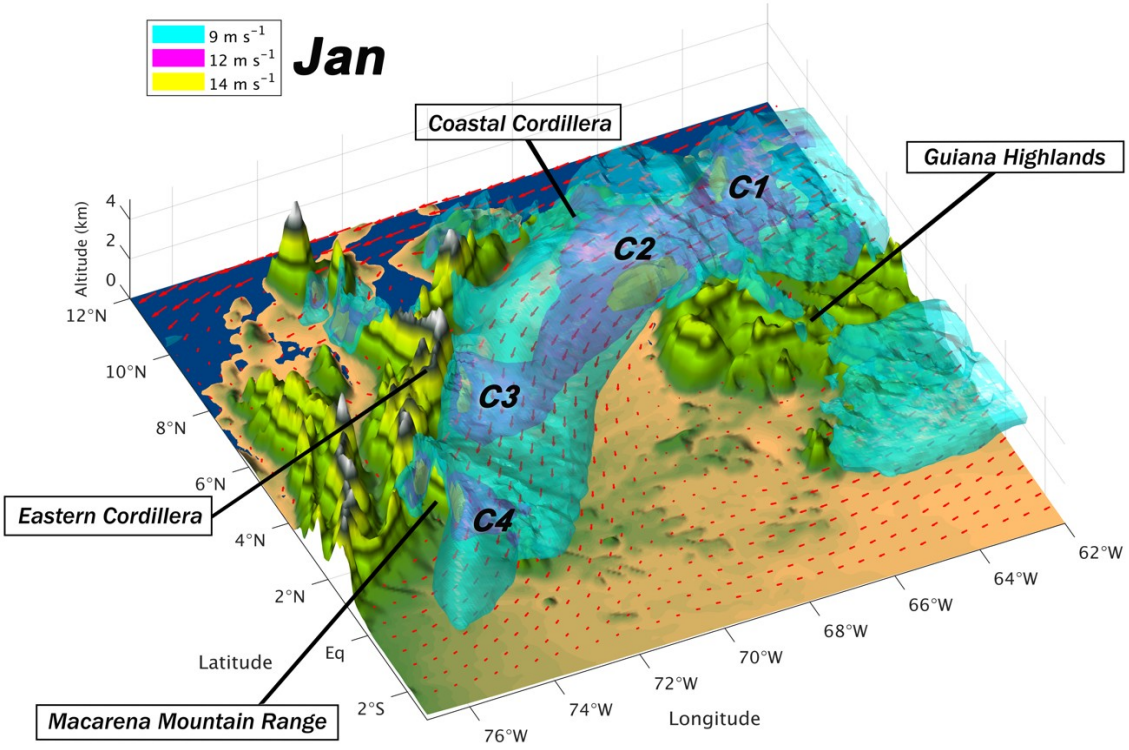

Figure 2. OLLJ-3D mean structure during January 2014, showing wind speed stream tubes of 9 m s^{-1} (cyan), 12 m s^{-1} (magenta) and 14 m s^{-1} (yellow) [instead of 8 m s^{-1}, a threshold of 9 m s^{-1} is used to improve clarity]. Interactions with surrounding topography produce localized cores of higher wind speeds (C1–C4). Lowland wind vectors at 500 m AGL are displayed in red.

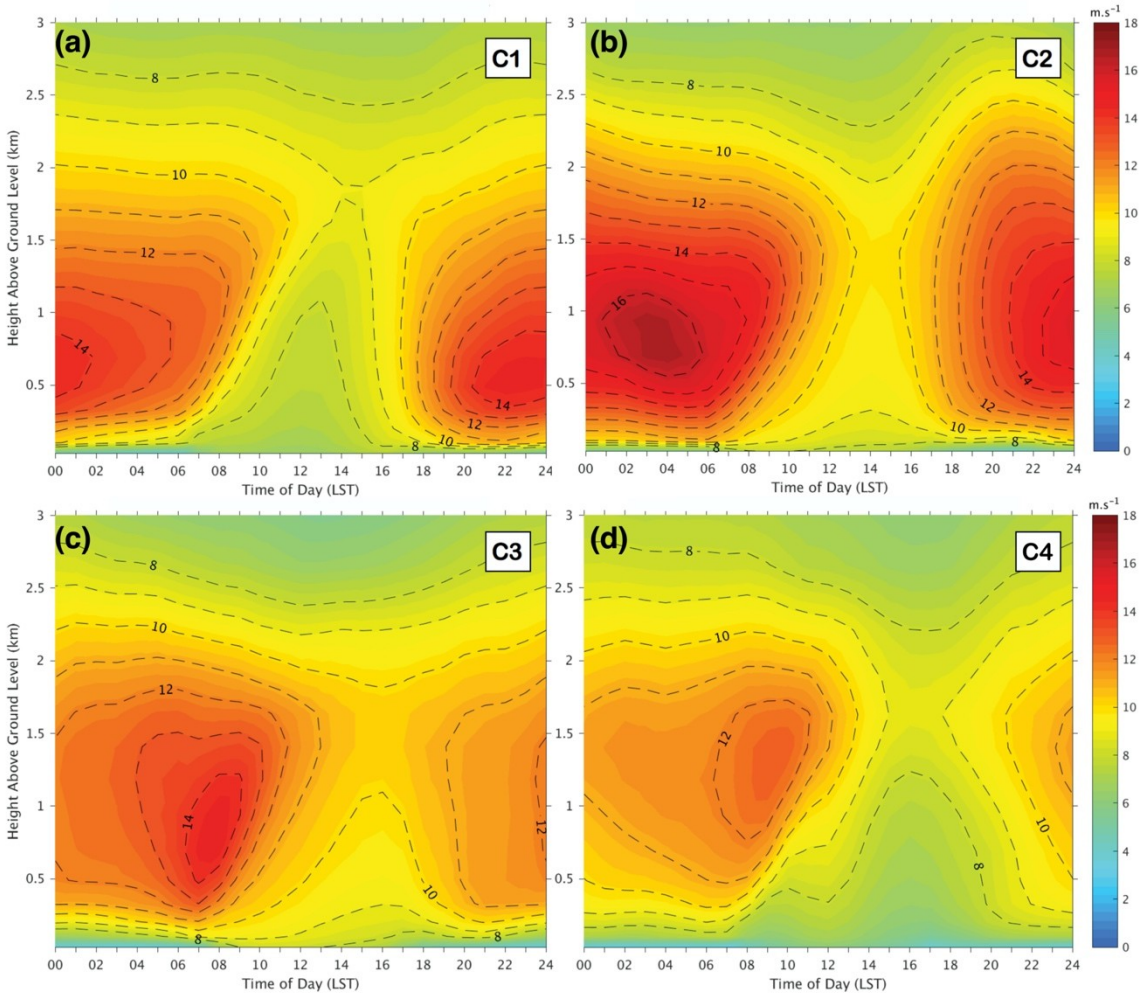

Figure 3. Time-height plot of hourly mean wind speeds from November 2013–March 2014 at each core location: (a) C1, (b) C2, (c) C3, and (d) C4. The differences in the time of occurrence of the maximum wind speed indicate an acceleration of the OLLJ in the streamwise direction.

The difference in time of occurrence of the diurnal maxima mean wind speeds at the center of each core location (Fig. 3), shows that there is an acceleration of the wind in the streamwise direction, with the maximum mean wind speed occurring at C1 around 2300 LST and C2 around 0400 LST. In contrast, at C3 and C4, the maxima mean wind speeds start approximately at 0700 LST and 0900 LST. The mean wind speeds are a minimum everywhere in the afternoon (~8 m s^{-1}, 1300–1600 LST). Table 1 summarizes the main characteristics of the OLLJ cores.

Based on the traditional mechanisms for LLJ formation (i.e., the Blackadar and Holton mechanisms), the acceleration of the wind should occur almost simultaneously at all locations once the upper-boundary-layer wind decouples from the surface layer; statically stabilized via radiative cooling, this layer impedes the upward propagation of frictionally retarded air. However, in the hourly 950–800-hPa-layer streamwise-acceleration field [$\partial V_s / \partial t$ in Eq. (1)]

178 (Fig. 4) it can be seen that acceleration is not uniform across the domain; rather, there are distinct
179 areas of acceleration coming from the Atlantic Ocean, the Caribbean Sea, and the Coastal
180 Cordillera. Additionally, even though these mesoscale pockets of acceleration propagate in the
181 streamwise direction, the C1–C4 wind-speed cores do not exhibit any propagation, just diurnal
182 intensification (as shown in Fig. 3); they occur at precise locations (Fig. 2, Table 1).
183

Table 1. Mean characteristics of the OLLJ cores.

	Core 1 (C1)	Core 2 (C2)	Core 3 (C3)	Core 4 (C4)
Geographical position	Guanipa Mesa, Venezuela	Santos Luzardo National Park, Venezuela	Fortul, Colombia	La Macarena, Colombia
Center location	9.5°N– 64.2°W	7.5°N– 67°W	5°N– 72°W	2°N– 73.5°W
Mean altitude (AGL)	~ 500 m	~ 700 m	~ 700 m	~ 1250 m
Maximum diurnal wind speed	~ 15 m s^{-1}	~ 17 m s^{-1}	~ 15 m s^{-1}	~ 13 m s^{-1}
Time of maximum wind speed	2300 LST	0400 LST	0700 LST	0900 LST

184 It is proposed herein that the OLLJ is the result of four mechanisms acting together to
185 accelerate the wind over the valley of the Orinoco River basin, producing a single wind structure
186 that extends from the Orinoco delta to the Amazon forest. The four mechanisms, depicted in
187 Fig. 5, involve (i) a sea-breeze penetration over the Orinoco River delta and Unare River
188 depression, (ii) katabatic flow down the Coastal Cordillera, (iii) three expansion fans from point
189 wakes in topography, and (iv) diurnal variation of turbulent diffusivity.
190

191 **3.1 Sea-breeze penetration**

192 Sea breezes generated at the coastline along the Atlantic Ocean and the Caribbean Sea
193 penetrate inland through the Orinoco River delta and Unare River depression. The relatively
194 cool maritime air behind the sea-breeze fronts (SBF) is advected to the basin interior and acting
195 as gravity currents cause the wind to accelerate (i.e., the two mesoscale regions of positive
196 acceleration at ~9ºN between 64ºW–66ºW in Fig. 4d). In the analysis, the maritime air is
197 characterized by mixing ratios greater than 14 g kg^{-1}.
198

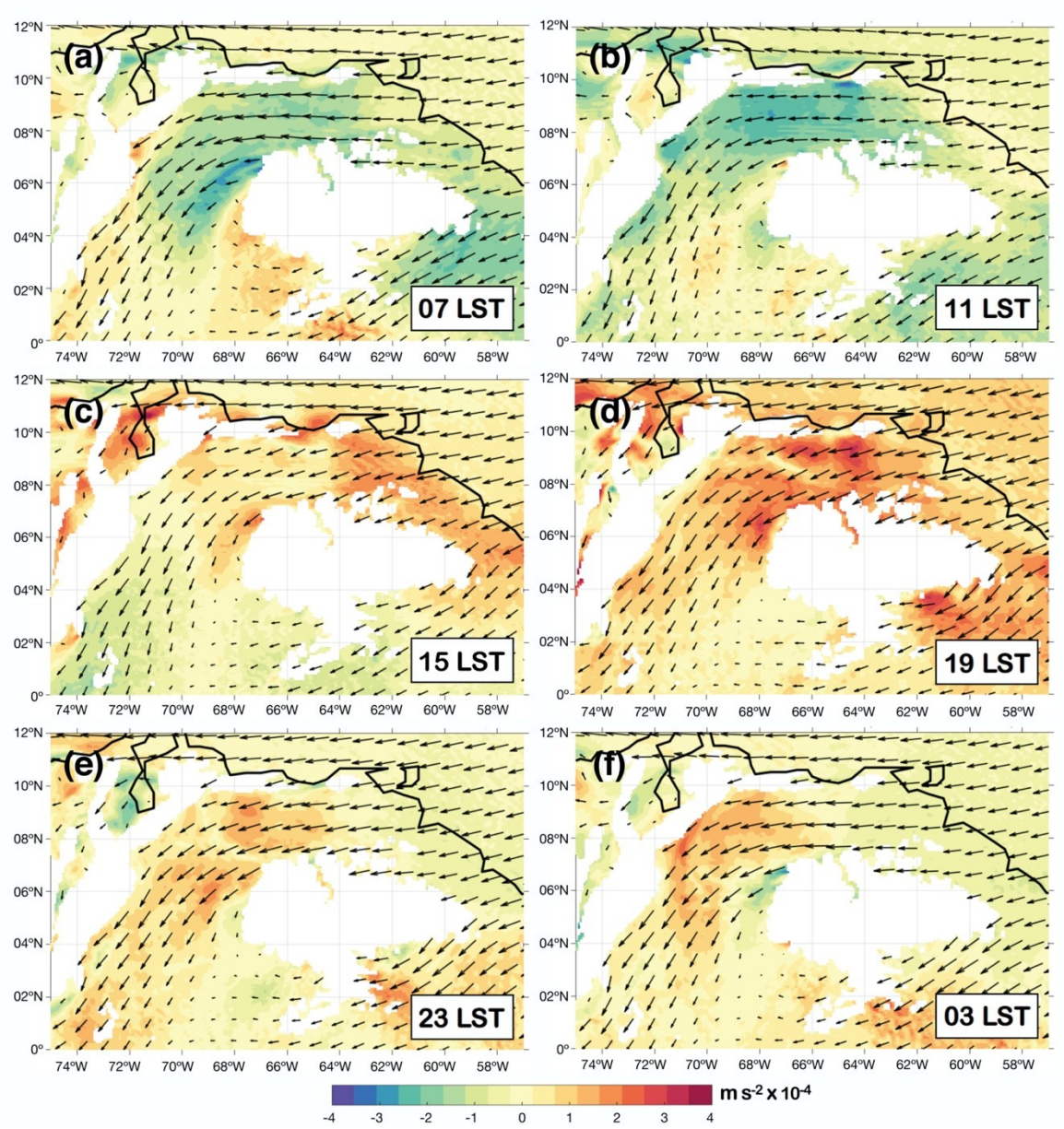

Figure 4. Diurnal variation of the 950–800-hPa-mean streamwise acceleration (shaded, m s^{-2} × 10^{-4}) and wind vectors from November 2013–March 2014: (a) 0700 LST, (b) 1100 LST, (c) 1500 LST, (d) 1900 LST, (e) 2300 LST, (f) 0300 LST. Warm (cold) colors indicate acceleration (deceleration) of the wind.

3.1.1 Orinoco delta region

The diurnal cycles of mean wind speed and potential temperature (Fig. 6) along the Orinoco delta region and Venezuelan Llanos (axis of propagation M in Fig. 5), show the sea breeze already established at 1100 LST (Fig. 6b), with a well-defined thermal internal boundary layer to the east of 64ºW; an indication that cool maritime air has advanced over the Orinoco delta region. As the day progresses, this denser air is advected further onshore, and once it

reaches the western limit of the Guanipa Mesa (~64.5ºW) around 1500 LST (Fig. 6c), it flows downslope causing the wind to accelerate.

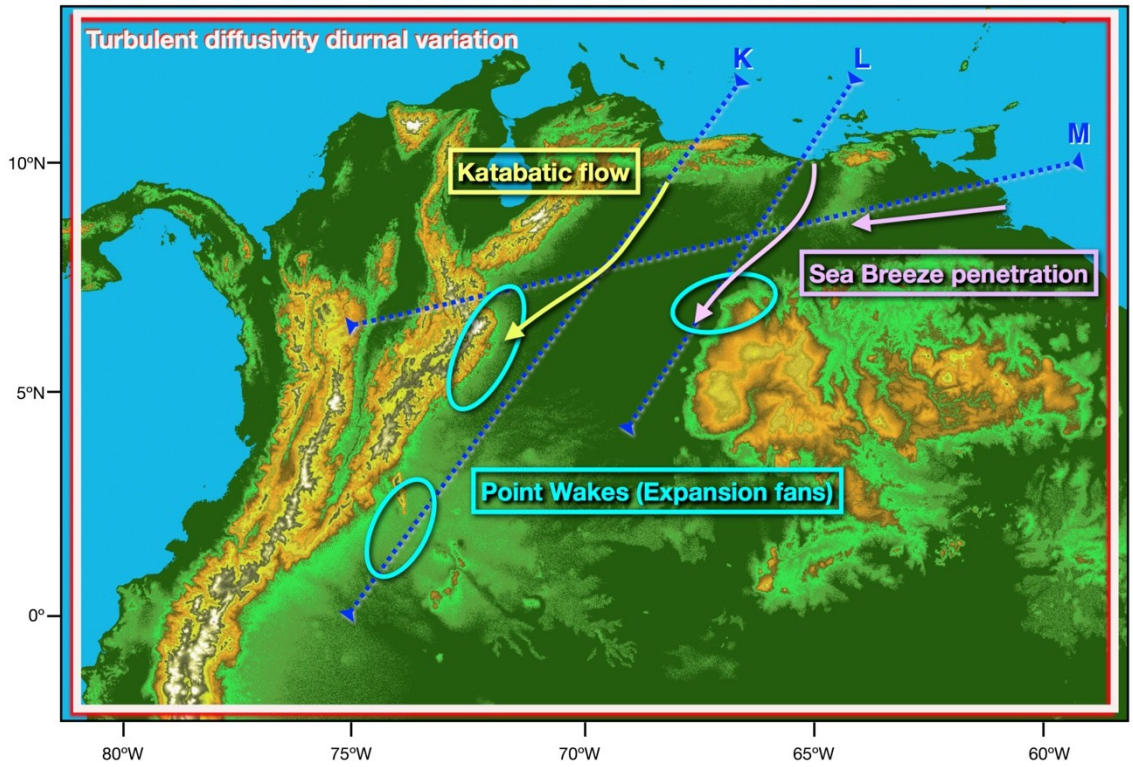

Figure 5. Locations of the four mechanisms causing the OLLJ. The limits of the cross sections along the axis of propagation of the Orinoco Delta (M) and Unare River (L) sea breezes, and Coastal Cordillera katabatic flow (K) are shown by dark blue dashed lines.

Because energy is conserved along an isentrope in dry-adiabatic motions [i.e., d(h + gz)/dt = 0, where $h = C_p \theta$ is the enthalpy], the acceleration of the wind, and consequently formation of the first OLLJ core (C1), is attained by transformation of potential energy into kinetic energy as the air on top of the Guanipa Mesa loses height downstream (see the bending isentropes at C1 locations in Fig. 6). A simple energy-transformation calculation for near midnight, using reduced gravity to account for the buoyancy effects opposing the gravitational force, yields just a –3 m s^{-1} difference with the wind speed given by the model, even though the nonhydrostatic effects of pressure were not considered.

The diurnal cycle of different surface variables at a selected point over the Guanipa Mesa (8.9ºN– 64.5ºW), shows evidence of the gravity-current nature of the sea breeze (Fig. 7). Starting at 1500 LST, a drop in potential temperature occurs, while there is an increase in surface pressure and mixing ratios. These are characteristics typical of the passage of a cool maritime density current (Simpson, 1987, 1994).

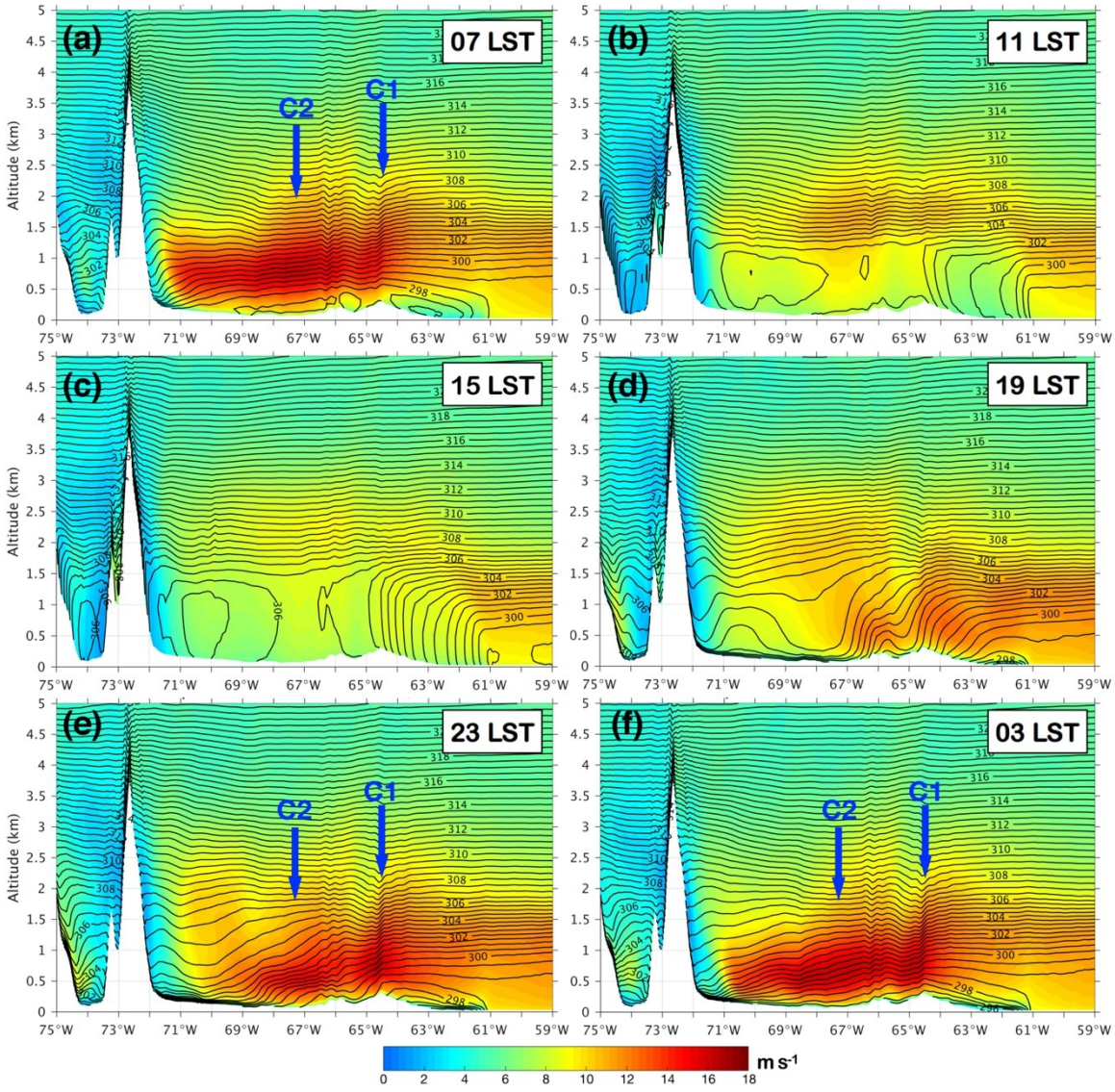

Figure 6. Diurnal variation of mean wind speed (shaded, m s^{-1}) and potential temperature (contoured, K), from November 2013–March 2014, in a vertical cross-section along the axis of propagation M (Fig. 5) at: (a) 0700 LST, (b) 1100 LST, (c) 1500 LST, (d) 1900 LST, (e) 2300 LST, (f) 0300 LST. The relative positions of the C1, C2 cores are also shown. Potential temperatures are contoured in 0.5 K increments.

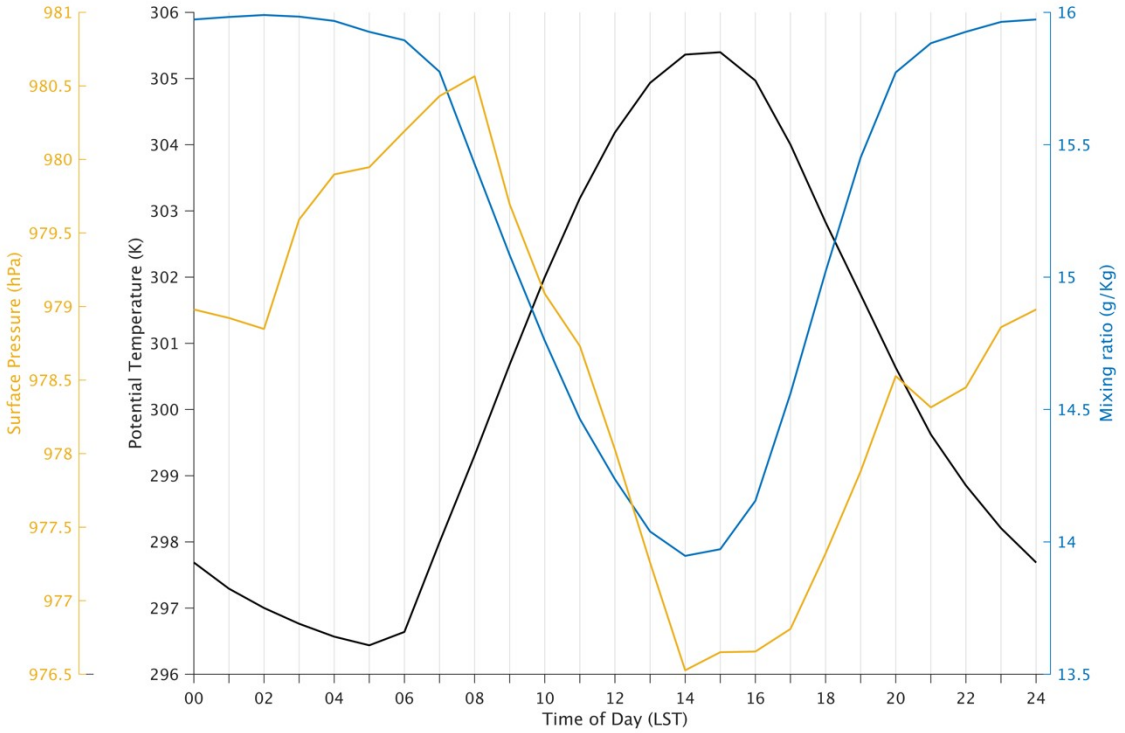

Figure 7. Diurnal cycle of surface pressure (yellow, hPa), potential temperature (black, K), and mixing ratio content (blue, g kg^{-1}), from November 2013–March 2014, at a surface location (8.9ºN– 64.5ºW) over the Guanipa Mesa (Venezuela).

223

224 **3.1.2 Unare River depression**

225 The Unare River depression is the ~100-km gap in the Coastal Cordillera that allows the
226 river to discharge into the Caribbean Sea. This depression is connected to the Venezuelan
227 Llanos and, because of the lack of prominent topographic features along its corridor (axis L in
228 Fig. 5), enables the inland penetration of the sea breeze created therein. Based on an analysis of
229 satellite imagery, Foghin-Pillin (2016) showed that this sea breeze penetrates up to 250 km in an
230 SSW direction.

231 A well-established SBF around 10ºN (Fig. 8b), separating the cool maritime air from the
232 statically-unstable mixed layer over the Llanos, starts advancing onshore around 1300 LST and
233 reaches the limits of the Guiana Highlands (~ 7ºN) ten hours later (Fig. 8e); which implies a
234 propagation speed of 8.3 m s^{-1}. Interestingly, gravity current theory predicts that under these
235 atmospheric conditions the sea breeze should propagate at that very same speed. Once the cool
236 air that has been accelerating behind the SBF arrives at the location of the C2 core (Fig. 5 and
237 Fig. 8a, e, f), it merges with the latter so increasing the localized wind speed.

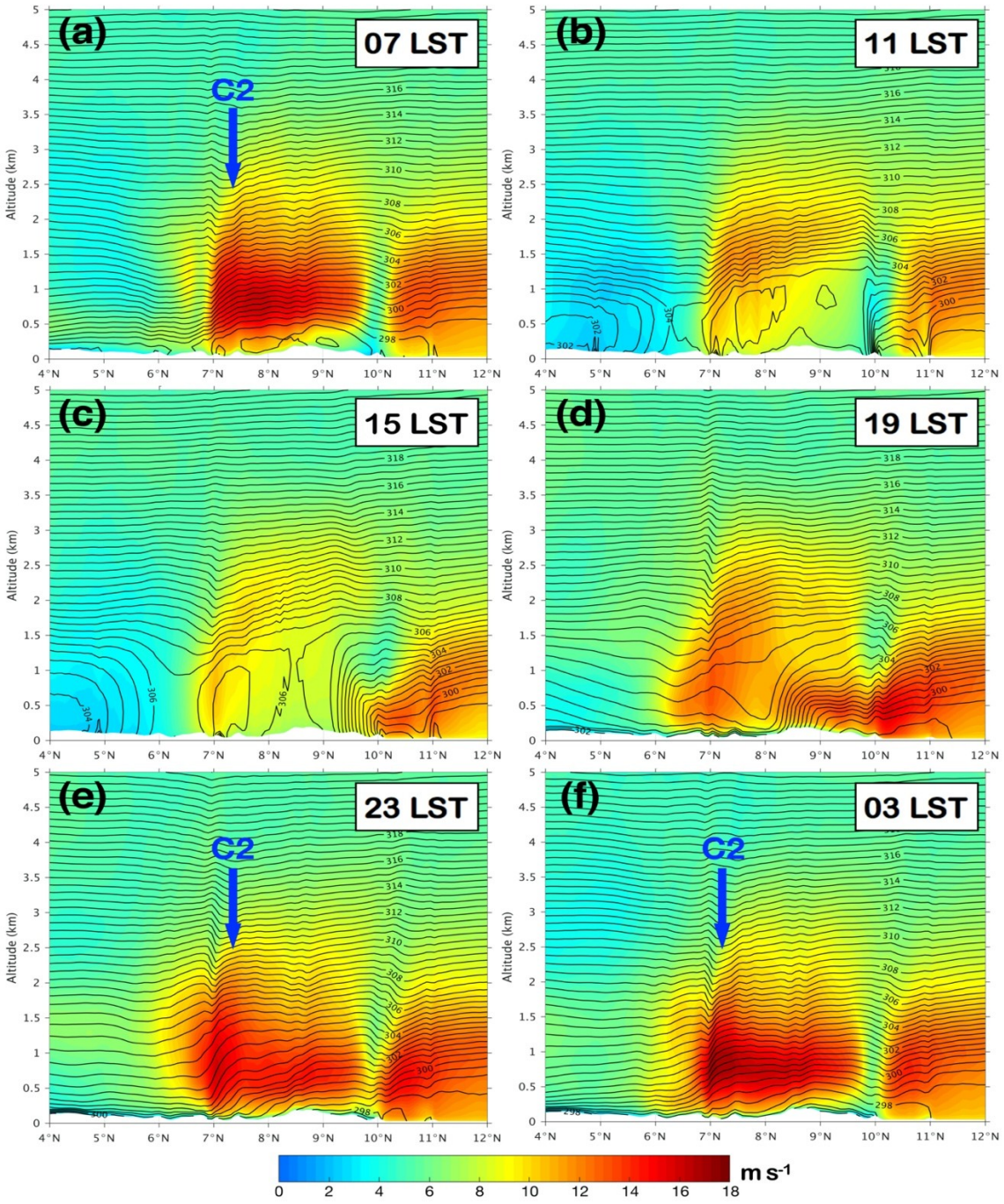

Figure 8. Diurnal variation of mean wind speed (shaded, m s^{-1}) and potential temperature (contoured, K), from November 2013–March 2014, in a vertical cross-section along the axis of propagation L (Fig. 5) at: (a) 0700 LST, (b) 1100 LST, (c) 1500 LST, (d) 1900 LST, (e) 2300 LST, (f) 0300 LST. The relative position of the C2 core is also shown. Potential temperatures are contoured in 0.5 K increments.

Impacts of the penetration of the sea breeze on the behavior of surface variables at a selected location (8ºN– 66.5ºW) along its axis of propagation L, can be assessed from Fig. 9, where starting at 1900 LST with the arrival of the SBF, there is a sudden increase in wind speed and a change in its direction from ENE to a less zonal NE (Fig. 9a). The southward advance of the sea breeze causes the rapid increase in the negative meridional component of the wind ($-v$) and the decrease in magnitude of the easterly component ($-u$). At the same time, the mixing ratio content and surface pressure exhibit a similar increasing rate of change, while the potential temperature continues dropping with a slight variation on its rate of change (Fig. 9b).

Therefore, the Unare sea breeze exhibits all the characteristics of a gravity current as proposed by Simpson (1987), Koch & Clark (1999), and Koch et al. (2005), namely:

- The observed (8.4 m s^{-1}; Foghin-Pillin, 2016) and modeled speed of propagation (8.3 m s^{-1}) are consistent with that predicted from gravity current theory (C_{gc}= 8.3 m s^{-1}),
- there is a continuous cooling of the surface after the arrival of the SBF,
- a permanent rise in surface pressure, and
- the wind changes direction with an increase in speed.

Some of the instantaneous or short-lived shifts (i.e., rises or drops) expected in temperature and surface pressure upon the arrival of the SBF, cannot be determined due to the current specifications of the model. An even finer spatial and temporal resolution (< 1-km grid spacing and one-minute outputs) is needed to analyze this phenomenon with enhanced detail.

Stratified fluid dynamics also predicts that the intrusion of a gravity current into a less dense, two-layer, stably stratified fluid system, as the one existing ahead of the SBF at 1900 LST (Fig. 8d), may generate wave-like perturbations (e.g., bores, solitons), as occurs in Australia's Gulf of Carpentaria (e.g., Clarke et al., 1981; Goler & Reeder, 2004; Reeder et al., 2013; Smith et al., 1982) and other parts of the world (e.g., Coleman et al., 2010; Koch & Clark, 1999; Tsai et al., 2004; Watson & Lane, 2016). However, the Unare sea breeze does not spawn such perturbations because the depth of the gravity current is much larger (~ 5 times) than the thickness of the stable-stratified boundary layer being perturbed. In this case, the latter is mixed into the gravity current, causing it to behave as if the lower layer does not exist (Simpson, 1987).

Furthermore, according to Koch & Clark (1999)—based on the modeling work of Haase & Smith (1989)—one of two parameters that determine if a bore can be generated from the intrusion of a gravity current is the ratio (μ) of the long gravity wave phase speed (C_o) to the gravity current speed (C_{gc}) [Eq. (3)], where N is the Brunt-Väisälä frequency, and h_o is the depth of stratified-boundary-layer inversion.

$$\mu = \frac{C_o}{C_{gc}} = \frac{2 N h_o / \pi}{C_{gc}} > 0.7 \qquad (3)$$

For the Unare sea breeze, the calculated nondimensional value of $\mu = 0.28$ indicates that the flow is in the "supercritical regime" where the gravity current propagates faster than any gravity waves so that no bores can be generated. The ratio μ is calculated for 2000 LST when the stratified boundary layer ahead of the SBF is well established.

279
280

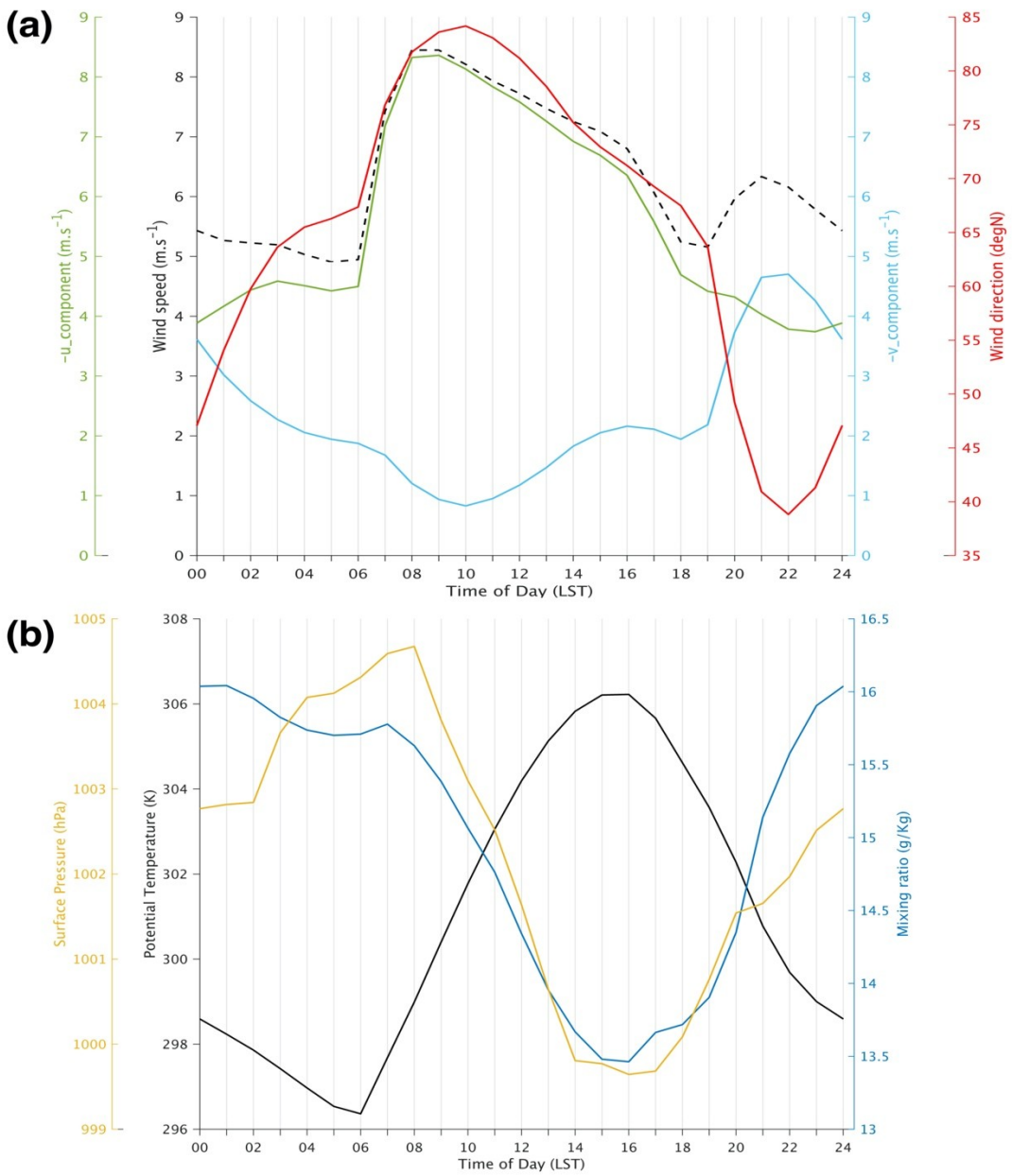

Figure 9. Diurnal cycle of (a) wind direction (red, degN), wind speed (dashed, m s^{-1}), zonal wind speed (green, m s^{-1}), meridional wind speed (cyan, m s^{-1}), and (b) surface pressure (yellow, hPa), potential temperature (black, K), and mixing ratio content (blue, g kg^{-1}), from November 2013–March 2014, at a selected surface location (8ºN– 66.5ºW; Aguaro-Guariquito National Park, Venezuela) along the axis of propagation L (Fig. 5). The zonal and meridional wind speeds are negative (easterly and northerly components, respectively).

3.2 Katabatic flow

The contribution to the OLLJ streamwise acceleration coming from the Coastal Cordillera (i.e., mesoscale area of positive acceleration at ~9ºN– 68.5ºW in Fig. 4d) has its origin in two factors: the radiative cooling of the southern slope near sunset, which produces shallow density currents; and the advection of cool maritime air over the top of the ridge. The diurnal variations of potential temperature and mean wind speed along the axis of propagation K (Fig. 10), show that the combination of these two factors starting around 1500 LST (Fig. 10b), cools down the hillside enough to generate a fast, cold downslope flow similar to that of a Bora phenomenon (Stull, 2015b; Fig. 10c–f). The maximum wind speed over the lee slope (13 m s^{-1}) is attained at 2300 LST (Fig. 10e). Because the flow is supercritical (Froude Number = 2.4), once it reaches the lowlands it creates a nocturnal hydraulic jump, as suggested by the curved isentropes over the southern flank of the mountain (Fig. 10d–f).

As cool air continues flowing downslope the Coastal Cordillera, it acts as a gravity current with a leading edge around 9.2ºN at 1900 LST (Fig. 10d) that propagates up-valley during the night, weakening near 6ºN– 72ºW at 0200 LST (not shown) once it encounters a point wake in the Eastern Cordillera. Hence, this density current exhibits a ground speed of ~14 m s^{-1}, which results from the combination of the depth and magnitude of the negatively buoyant air (C_{gc} 5 m s^{-1}), and the background wind speed (~9 m s^{-1}). The streamwise-acceleration area that follows this gravity-current leading edge ends up merging at 0300 LST around 7ºN– 70ºW with the trailing acceleration pocket originated by the sea breezes (Fig. 4f).

Evidence for this katabatic flow having the characteristics of a gravity current proposed by Simpson (1987), Koch & Clark (1999), and Koch et al. (2005), is given in Fig. 11, which shows the diurnal cycle of the wind field, potential temperature, surface pressure, and mixing ratio at a selected surface location (7.5ºN– 69.7ºW) along the axis of propagation K (Fig. 5). With the arrival of the gravity current at around 2200 LST, there is an increase in wind speed and a small change in its direction (Fig. 11a); meanwhile, a change in the rate of nocturnal cooling with a corresponding change in the increasing surface pressure rate is produced (Fig. 11b). The sustained increase in mixing ratio indicates the maritime origin of the gravity current.

In a similar way to the Unare and Orinoco-delta sea breezes, as the katabatic flow propagates over the Llanos and the near-surface layer ahead of it stably stratifies (via nocturnal radiative cooling), the intrusion of this denser current could generate waves in the form of bores or solitary waves. However, the evaluation of the ratio μ [Eq. (3)] yields a value of 0.12, so indicating that flow is supercritical, and no waves can be spawned.

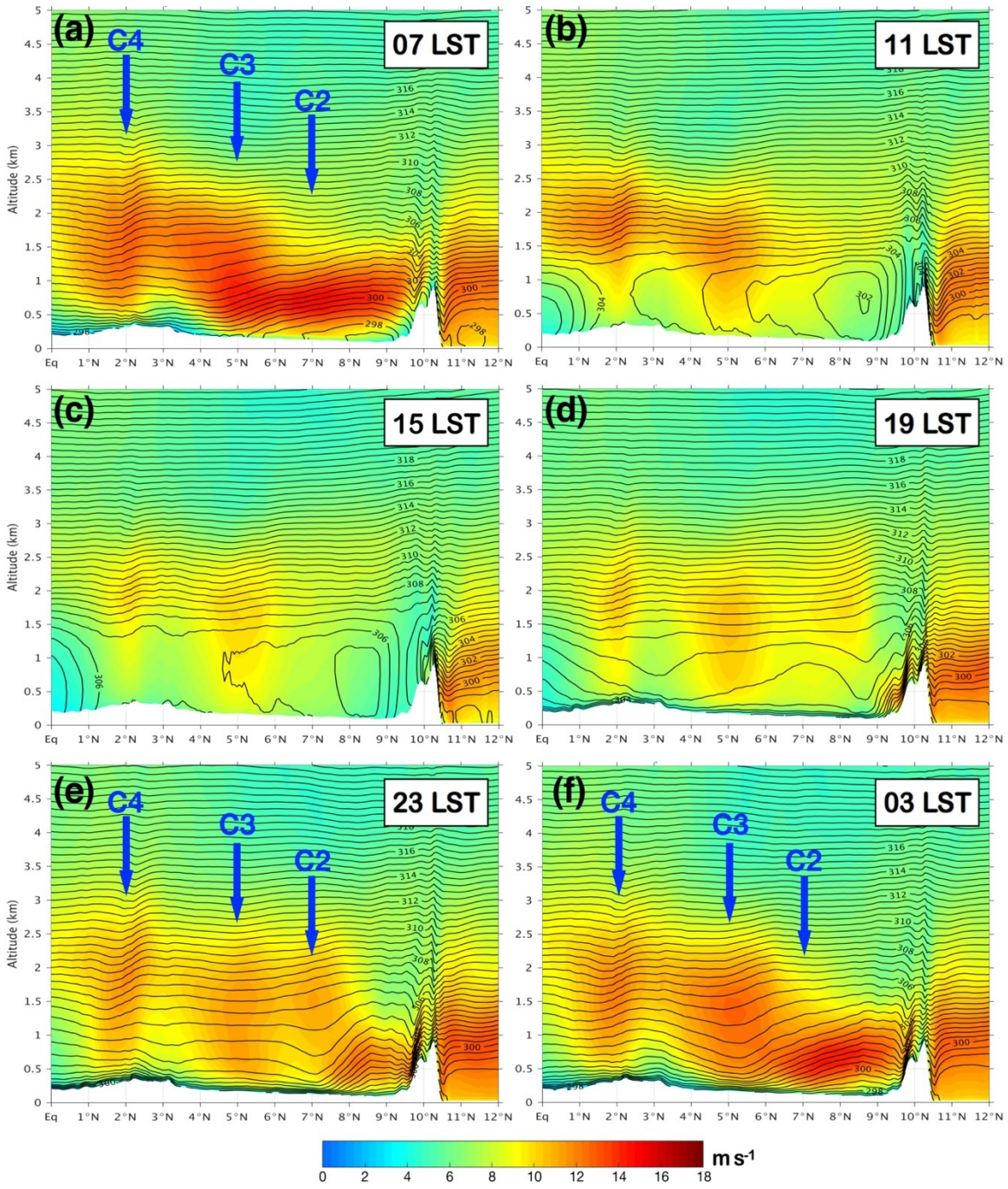

Figure 10. Diurnal variation of mean wind speed (shaded, m s^{-1}) and potential temperature (contoured, K), from November 2013–March 2014, in a vertical cross-section along the axis of propagation K (Fig. 5) at: (a) 0700 LST, (b) 1100 LST, (c) 1500 LST, (d) 1900 LST, (e) 2300 LST, (f) 0300 LST. The relative positions of the C2–C4 cores are also shown. Potential temperatures are contoured in 0.5 K increments.

316

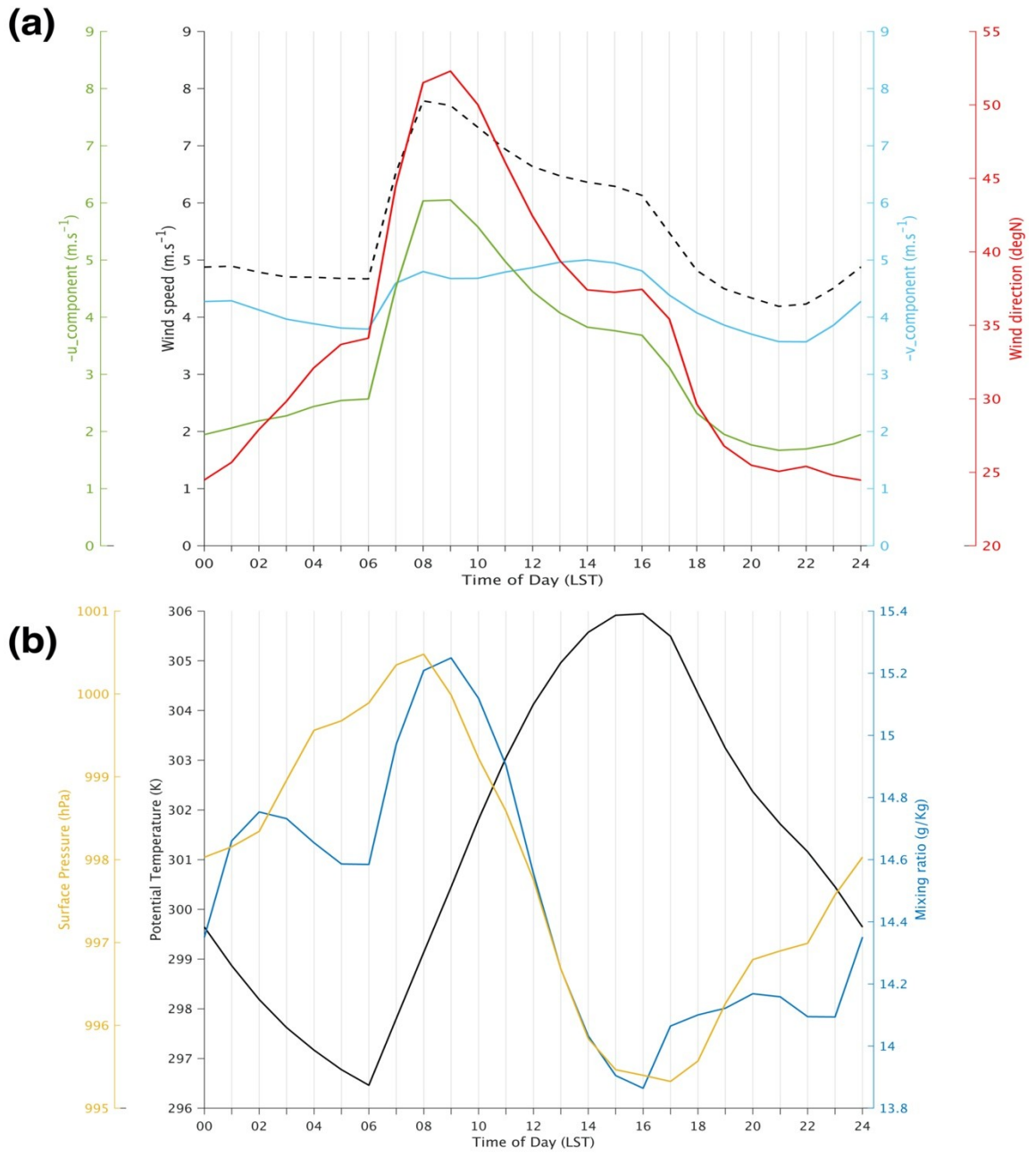

Figure 11. Diurnal cycle of (a) wind direction (red, degN), wind speed (dashed, m s^{-1}), zonal wind speed (green, m s^{-1}), meridional wind speed (cyan, m s^{-1}), and (b) surface pressure (yellow, hPa), potential temperature (black, K), and mixing ratio content (blue, g kg^{-1}), from November 2013–March 2014, at a selected surface location (7.5ºN– 69.7ºW; Las Mulas, Apure-Venezuela) along the axis of propagation K (Fig. 5). The zonal and meridional wind speeds are negative (easterly and northerly components, respectively).

317

3.3 Point wakes and expansion fans

Previous studies have shown that supercritical-channel-flow hydraulic theory can be used to explain particular accelerating flow regions associated with bending topography in coastal environments (Juliano et al., 2017; Patricola & Chang, 2017; Samelson, 1992; Söderberg & Tjernström, 2001; Winant et al., 1988). Since the OLLJ is a channeled flow bounded by topography and capped by the inversion at the top of the planetary boundary layer (PBL), the same hydraulic theory arguments are used herein to explain the preferred location of some of the OLLJ cores.

In a channel flow—represented by a two-layer shallow water model in which the lower layer is the PBL and the upper layer is the free troposphere—the ratio of the flow velocity to the speed of long gravity waves on the interface (i.e., the Froude Number, Fr) will determine the behavior of the flow when the vertical boundaries expand or contract. When Fr is supercritical (i.e., $Fr > 1$), because the speed of the flow is faster than the speed of any gravity wave generated, the effect of a change in the geometry of the channel cannot be communicated upstream, and all the information travels downstream in the mean flow. Thus, if the lateral boundary of the channel (e.g., shoreline topography, mountains) turns away from the mainstream, a hydraulic expansion fan is induced downwind, whereas if it turns closer to the flow, it produces a hydraulic compression jump.

Points (terrain prominences) along bounding topography mark the locations where the flow separates from the terrain—producing low-speed point wakes—or if under supercritical conditions remains attached to it, where expansion fans are generated. The characteristics of an expansion fan downwind of a point wake are lateral spreading of the flow, decrease in thickness of the PBL, and accelerating flow as a result of the conservation of the Bernoulli function (Patricola & Chang, 2017; Samelson, 1992; Söderberg & Tjernström, 2001; Winant et al., 1988; Young & Winstead, 2005). On the other hand, a low-speed point wake can be recognized as an extended region of low wind trailing downwind from the point (Young & Winstead, 2005).

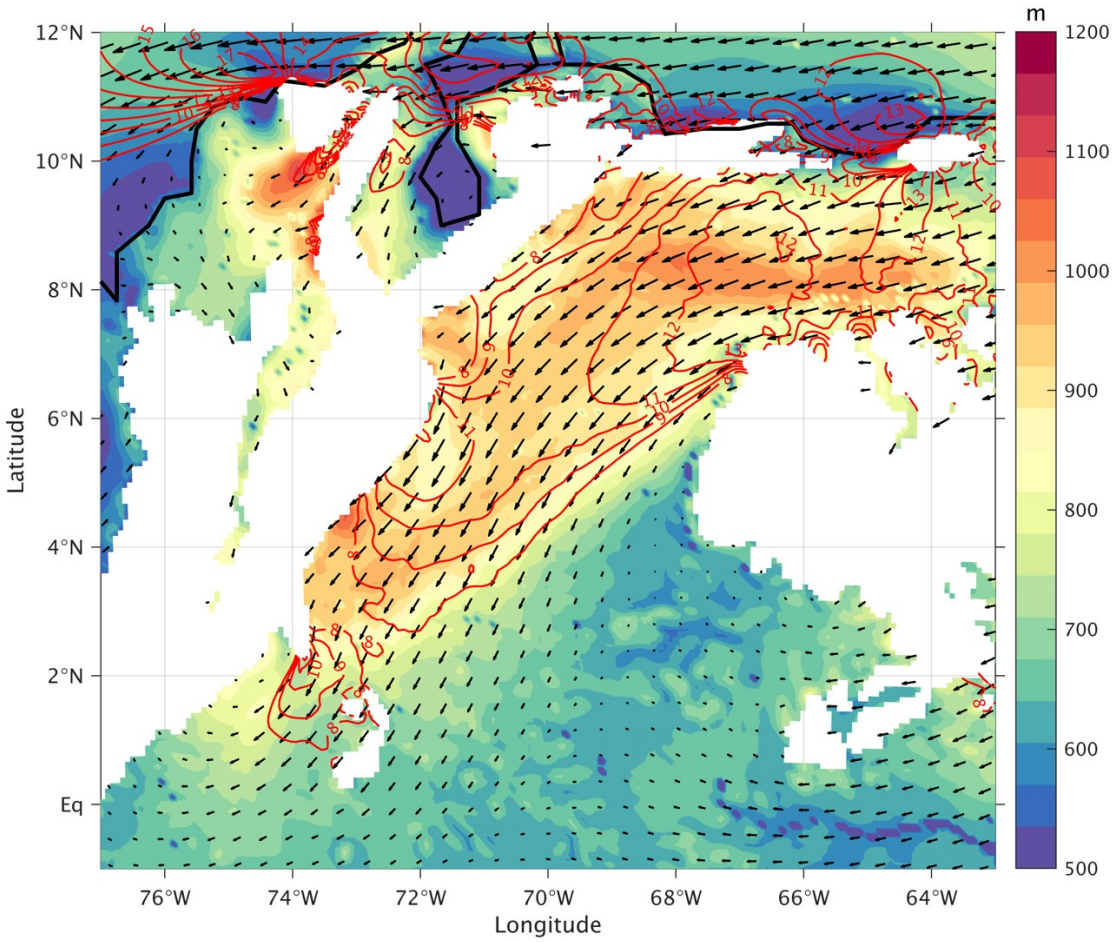

Figure 12. Horizontal characterization of mean diurnal PBL height (shaded, m AGL) and mean wind field during November 2013–March 2014. Isotachs (red, m s^{-1}) and velocity vectors at 500 m AGL. Wind speeds greater than 8 m s^{-1} are contoured in 1 m s^{-1} increments.

An illustration of the effect of expansion fans on the height of the PBL and, subsequently, on the wind speed, is depicted in Fig. 12, where the regions of maximum wind speed (closer to the surrounding topography) in the diurnal 500 m-AGL mean wind field coincide with the locations of low diurnal mean heights of the PBL along the OLLJ corridor. In the Orinoco River basin, as the large-scale wind flows through the valley, the main stream is deflected by bending terrain, producing point wakes at three specific locations: the Guiana Highlands (Cerro La Emilia), Eastern Cordillera (Cerro Umpara), and Macarena mountain range (refer to cyan areas in Fig. 5). The regions of enhanced wind speed associated with their corresponding expansion fans, produce the C2–C4 cores depicted in Fig. 4. A summary of the main features of the point wakes and their associated phenomena is indicated in Table 2.

According to supercritical-channel-flow hydraulic theory, *Fr* and the angular change in the flow direction due to the bending boundary ($d\theta$), predict the final flow wind speed and PBL height depending on:

$$\sin\beta = \frac{c}{U} = \frac{\sqrt{g' h}}{U} = \frac{1}{Fr} \quad (4)$$

$$\frac{dU_n}{d\theta} = \frac{-U_n}{\cos\beta} \quad (5)$$

$$\frac{dU_n}{dh} = \frac{-g'}{U_n} \quad (6)$$

$$\frac{U^2}{2} + g' h = B \quad (7)$$

Where β is the angle of the expansion fan with respect to upstream flow, c is the gravity wave phase speed, U is the flow speed, g' is the reduced gravity, h is the PBL height, U_n is the component of the velocity normal to the wave that stems from the point where the boundary bends, and B is the Bernoulli function. The final depth of the PBL obeys the steady-state momentum equation [Eq. (6)], while the total velocity (if the flow is frictionless) follows Eq. (7).

Table 2. Main characteristics of the point wakes.

	Guiana Highlands	Eastern Cordillera	Macarena Mountain Range
Geographic feature	Cerro La Emilia	Cerro Umpara	Serranía de La Macarena
Location	7.2°N–66.3°W	6.6°N–71.8°W	2.5°N– 73.8°W
Angular flow deflection	~ –13°	~ –17°	~ –10°
Hydraulic effect	Expansion fan	Expansion fan	Expansion fan
Associated OLLJ core	C2	C3	C4
Hydraulic theory predicted final wind speed*	13 $\pm$ 1 m s^{-1}	12 $\pm$ 1 m s^{-1}	11 $\pm$ 1 m s^{-1}
Model final wind speed	~13 m s^{-1}	~12 m s^{-1}	11-12 m s^{-1}
Hydraulic theory predicted final PBL height*	560 $\pm$ 110 m	460 $\pm$150 m	600 $\pm$ 85 m
Model final PBL height	~600 m	~600 m	~650 m

**Uncertainties estimation procedure is presented in Appendix A.*

At the northwestern Guiana Highlands, the terrain is oriented approximately in an ENE–WSW direction (Fig. 12), although around 7.2ºN–66.3ºW (Cerro La Emilia) the terrain angles approximately 13º southward. Because the channel width increase is small, the flow remains attached to the terrain, and the first expansion fan is produced. Given the boundary layer

conditions upstream of the point wake, Eqs. (4)–(7) predict a PBL height downwind of ~600 m and a final wind speed of ~13 m s^{1} as the flow accelerates to negotiate the 13º expansion, which indeed occurs (Fig. 12). Further downstream, the mountainous topography ends sharply, causing separation of the flow from the terrain and the generation of a low-speed point wake. The combination of an expansion fan and a low-speed point wake is known as a compound point wake (Young & Winstead, 2005).

The wind speed core (C2) associated with this expansion fan is located over the Santos Luzardo National Park in Venezuela, where it may be responsible for the Llanos del Orinoco aeolian landforms of dune systems described by Tripaldi & Zárate (2016). Such landform modifications by the wind are so strong and permanent that they are clearly visible in satellite imagery.

The second expansion fan is generated by the Cerro Umpara (6.6ºN–71.8ºW) where an approximately northerly flow is deflected 17º westward. The base flow at this location is transcritical, a pattern described by Rogerson (1999) where the main stream is supercritical in the vicinity of orographic bends but it is subcritical upwind.

According to the conditions of the flow around Cerro Umpara, and the hydraulic theory summarized previously, downstream of the orographic bend the flow accelerates and reaches ~12 m s^{-1} while decreasing the height of the PBL to ~600 m (Fig. 12). Because the main stream flows parallel to the Eastern Cordillera, the wind speed core (C3) created by the expansion fan is found downwind, attached to the sloping terrain.

This low-level wind maximum remains attached to the mountain under the effect of Coriolis force and PGF, which generate a net inward acceleration that traps the wind against the terrain. The 950–800-hPa diurnal cycle of streamwise and crosswise forces in a 36 km × 36 km-box (around 5ºN–72.5ºW) near the hillside (Fig. 13), shows that during the day the crosswise PGF and Coriolis forces (Fig. 13b) act together to accelerate the wind towards the mountain, causing a positive crosswise acceleration from 0900 LST to 1600 LST. At night, as friction is turned off due to the statically stabilization of the lower troposphere, the total crosswise accelerations are closer to zero (~2100–0600 LST), and the streamwise acceleration component (Fig. 13a) becomes predominant. In this period, the advection is the driving term in the total streamwise acceleration because it has the fastest response to adjust to the changes occurring in the PGF (Outten et al., 2009).

As the wind continues flowing equatorward, it encounters the Macarena mountain range oriented north-south, so the low-level flow is diverted southward and runs attached to the terrain. The third expansion fan occurs when the bounding topography bends ~10º westward, thus causing an acceleration of the flow, and a decrease in the PBL height downstream (Fig. 12). The base flow at this location is also transcritical, and because of the accelerating flow, the wind speed reaches ~ 11 m s^{-1}, so giving origin to the last of four OLLJ cores (C4). Once the mountain ends, the flow separates from the terrain, and induces a low-speed point wake on the Macarena mountain range lee, while the expansion fan lies eastward of it.

Given the above, supercritical-channel-flow hydraulic theory reasonable explains the localized characteristics of the C2–C4 regions, also predicting their final wind speed and PBL height.

415

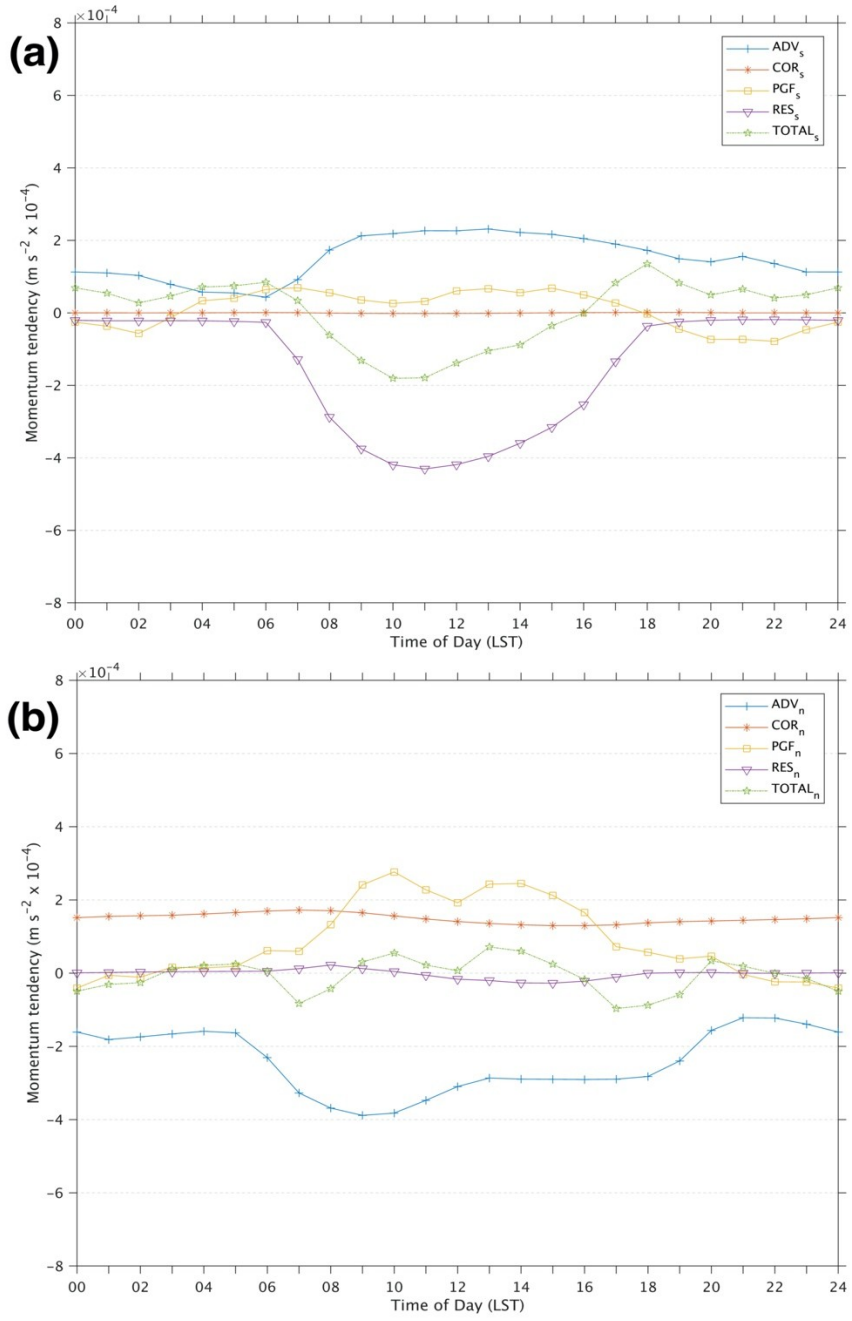

Figure 13. Diurnal cycle of the 950–800-hPa-mean (a) streamwise (*s*) and (b) crosswise (*n*) momentum balance components at the C3 region near sloping terrain (~5ºN–72.5ºW) during November 2013–March 2014. The advection (blue crosses), Coriolis (red asterisks), PGF (yellow squares), residual (purple triangles), and total (green stars) tendency terms in m s^{-2} × 10^{-4}.

3.4 Turbulent diffusivity diurnal variation

The Blackadar mechanism relies on the diurnal variation of turbulent diffusivity to produce an inertial oscillation of the horizontal wind, which eventually will generate the LLJ. Such inertial oscillation starts at sunset when turbulence diffusion in the boundary layer is reduced by static stabilization of the surface layer (via radiative cooling) so that frictionally retarded air is no longer transported upward, and the wind above becomes frictionless and accelerates. As the magnitude of the horizontal wind increases so does the Coriolis force, which makes the wind turn clockwise (counterclockwise in the Southern Hemisphere) and describe an oscillation around the geostrophic wind. At sunrise, radiative heating activates the turbulent mixing again, so friction adds to the force balance and the horizontal wind speed reduces to subgeostrophic values.

From a different perspective, this oscillation can be seen as the rotation of the ageostrophic wind in a circle centered on the geostrophic wind so that at some time during the night—which varies depending on the value of the Coriolis parameter *f* for each latitude—the ageostrophic wind has the same direction as the geostrophic wind. With both geostrophic and ageostrophic winds pointing in the same direction, the horizontal wind becomes supergeostrophic thus producing the LLJ.

In the hourly 950–800-hPa streamwise momentum balance at C1–C4 OLLJ cores (Fig. 14a–d), obtained by averaging a 45 km × 45 km box at the maximum wind speed location along 64ºW, 66.9ºW, 5ºN, and 1.5ºN respectively, the residual term (i.e., frictional effects) is the primary driving term causing total deceleration of the streamwise horizontal wind during daytime. On the other hand, during nighttime, when its value approaches close to zero (i.e., no frictional effects), the other forces in balance cause the positive streamwise acceleration of the wind. The latter is particularly true for the C3–C4 regions (Fig. 14c–d), whereas for the C1–C2 regions (Fig. 14a–b) the negative advection term shortens the total streamwise nocturnal acceleration cycle. The streamwise deceleration, initiated by the advection term at the C1–C2 regions, contributes to the early appearance of the maxima wind speeds, in comparison to the C3–C4 cores (Table 1), and is an indication of drainage flow (down valley) opposing the large-scale motions.

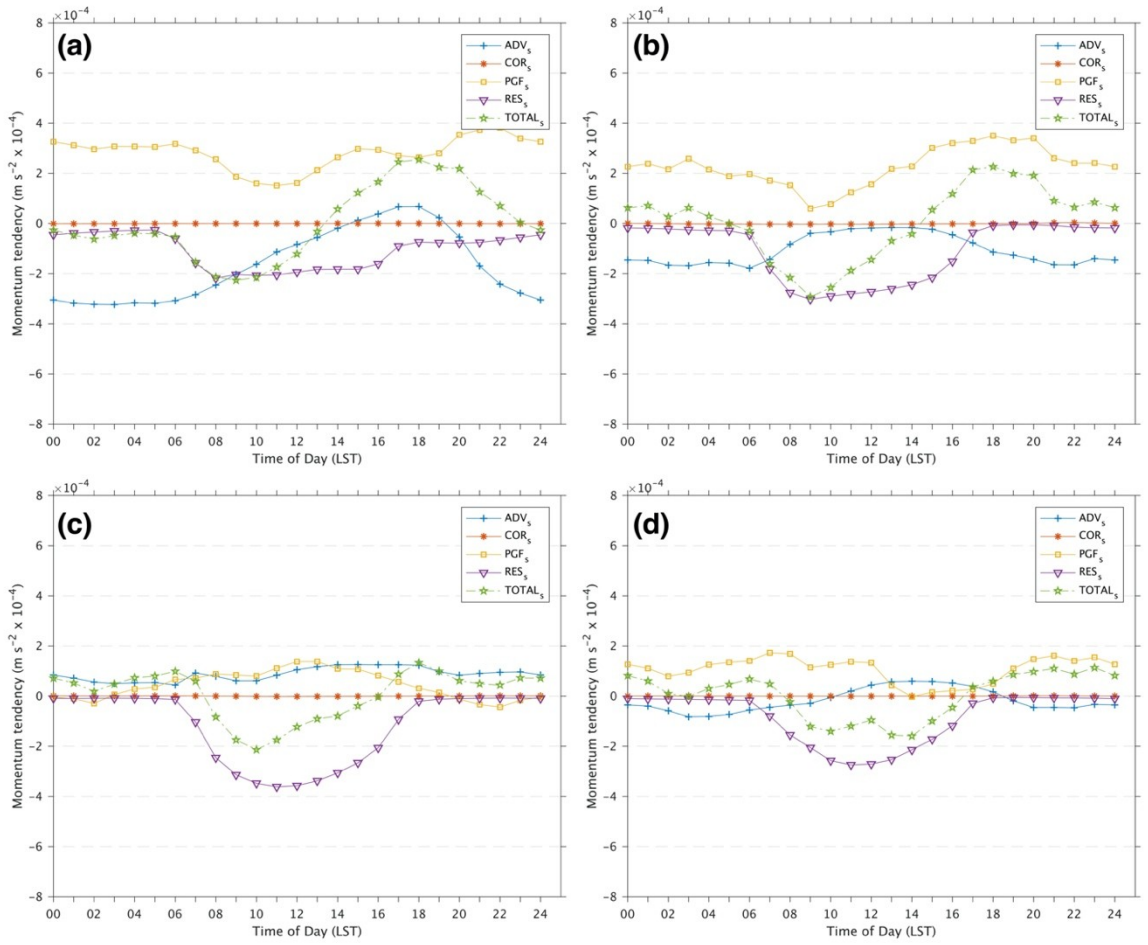

Figure 14. Diurnal cycle of the 950–800-hPa-mean streamwise momentum balance component during November 2013–March 2014 at (a) C1, (b) C2, (c) C3, and (d) C4 regions. The advection (blue crosses), Coriolis (red asterisks), PGF (yellow squares), residual (purple triangles), and total (green stars) tendency terms in m s^{-2} × 10^{-4}.

446

447 A supplemental illustration of the generalized effect of turbulent diffusivity diurnal
448 variation is depicted in Fig. 4, where frictional decoupling of the 950–800-hPa wind after sunset
449 cause the simultaneous streamwise acceleration of the flow over large areas across the domain
450 (Fig. 4d), whereas the activation of turbulent mixing during daytime induce the overall
451 deceleration of the wind (Fig. 4a, b). In a like manner, the diurnal evolution of the potential
452 temperature contours and mean wind speeds at different locations (Fig. 6, 8, and 10) show that
453 once the OLLJ has developed during nighttime (Fig. 6d–f, 8d–f, and 10d–f), the growth of the
454 daytime convective boundary layer erodes the LLJ from below diminishing its mean wind speed
455 (Fig. 6a–c, 8a–c, and 10a–c).

456 Interestingly, despite the turbulent diffusivity diurnal variation triggering the inertial
457 oscillation, so causing the clockwise rotation of the horizontal wind at each of the core locations
458 (not shown), the Blackadar mechanism does not strictly apply to all of them. The 950–800-hPa
459 streamwise and crosswise diurnal cycle of the mean horizontal, geostrophic, and ageostrophic

wind (Fig. 15), for the same locations as in Fig. 14, show that the maximum streamwise wind speed is the result of the combined streamwise geostrophic and ageostrophic winds at the C1 and C3 regions only (Fig. 15a, c), whereas the maximum wind speed in the C2 and C4 regions (Fig. 15b, d) results from a balance between the geostrophic and ageostrophic winds. In general, the horizontal wind in the C2 and C4 regions reflects such balance during the entire diurnal cycle. Moreover, the minimum wind speed is subgeostrophic at the C1 and C2 regions only, whereas it is supergeostrophic in the C3 and C4 regions. Strictly speaking, the minima wind speeds should be subgeostrophic everywhere, according to Blackadar's theoretical predictions.

Hence, the diurnal variation of turbulent diffusivity and subsequent inertial oscillation contribute to the OLLJ formation, although it plays a secondary role, especially close to the equator where the Coriolis parameter is so small that ageostrophic effects (e.g., changes in PGF due to terrain heating) drive the wind. The streamwise ageostrophic wind is, in general, of higher magnitude than the streamwise geostrophic wind in the C3 and C4 regions (Fig. 15c, d).

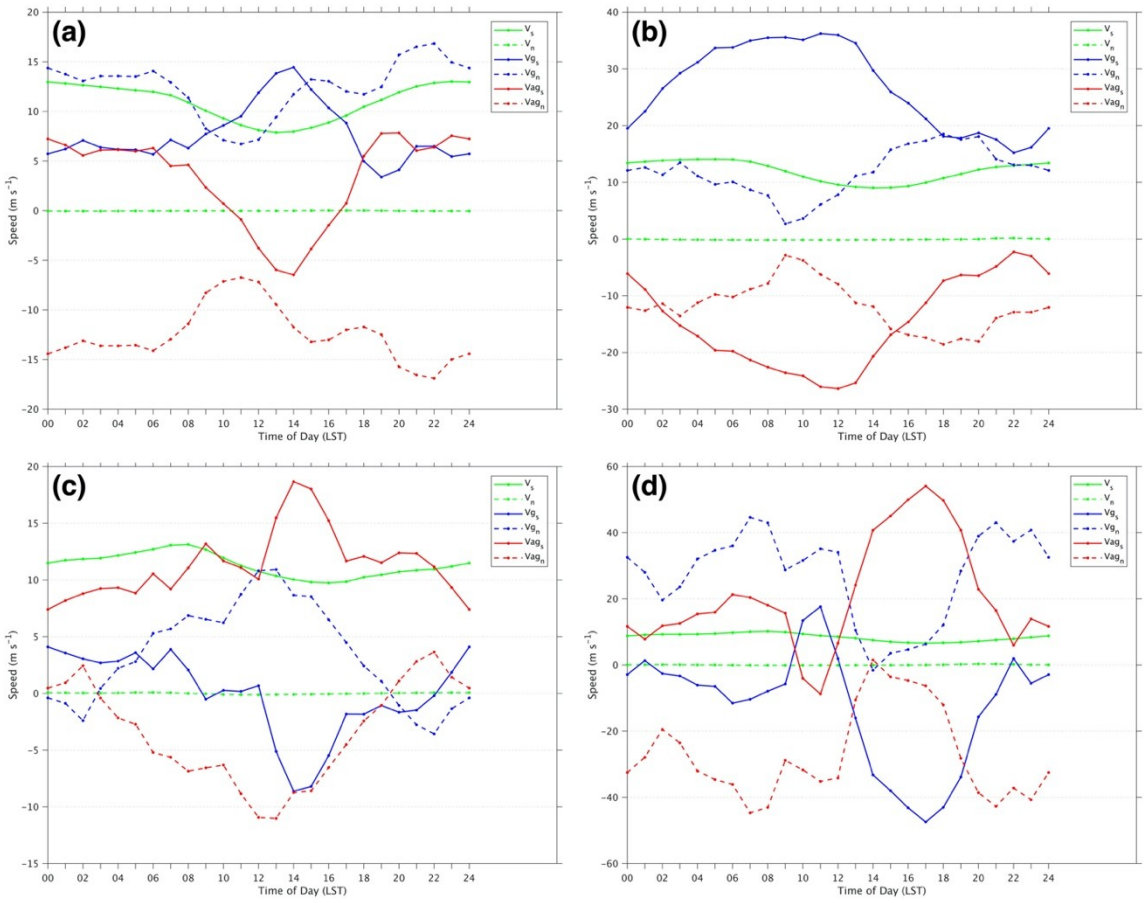

Figure 15. Diurnal cycle of the 950–800-hPa-mean streamwise (*s*) and crosswise (*n*) horizontal (green), geostrophic (blue), and ageostrophic (red) winds (m s^{-1}) during November 2013–March 2014 at (a) C1, (b) C2, (c) C3, and (d) C4 regions. Streamwise components in solid lines and crosswise components dashed. Geostrophic and ageostrophic crosswise components balance around zero m s^{-1} owing to the rotated coordinate system.

4 Summary and conclusions

Dynamical downscaling of the large-scale atmospheric conditions over northern South America, shows the presence of a low-level wind maximum occurring during the austral summer in the 950–800-hPa layer. This low-level wind maximum, herein identified as the Orinoco low-level jet (OLLJ), is a single stream tube (2000 km long × 300 km wide × 3 km deep, approximately) over Colombia and Venezuela, with mean wind speeds greater than 8 m s^{-1}. The OLLJ exhibits its seasonal maximum wind speed and largest spatial extent (2100 km × 450 km) in January, and its interaction with the surrounding topography produces four localized cores of higher wind speeds (C1–C4) along its curved axis of propagation.

In the diurnal cycle, the altitude of the cores increases in the streamwise direction (~500 m, 700 m, 700 m, and 1250 m AGL, respectively) under the influence of the sloped terrain. The maxima diurnal mean wind speeds (13–17 m s^{-1}) at each core location occur at different times during the night (2300, 0400, 0700, 0900 LST, respectively), thus showing an acceleration of the wind in the streamwise direction that starts in the Orinoco Delta and ends over the Amazon forest. The wind speeds are a minimum everywhere in the afternoon (~8 m s^{-1}, 1300–1600 LST).

Since acceleration of the flow is not uniform across the domain, as it is somewhat expected from the inertial oscillation and the topographic thermal forcing mechanisms, it is determined that the OLLJ is the result of four phenomena acting together to accelerate the wind over the valley of the Orinoco River basin, namely: the (i) sea breeze penetration over the Orinoco River delta and Unare River depression, (ii) katabatic flow down the Coastal Cordillera, (iii) three expansion fans from point wakes in the topography, and (iv) diurnal variation of turbulent diffusivity.

The continuous nocturnal advection of relatively cool air through the Orinoco delta region, Unare River depression (i.e., sea breezes penetration), and downslope of the Coastal Cordillera (katabatic flow), constitute a single density current that merges over the Llanos and propagates up-valley, causing acceleration of the wind behind its leading edge. Before combining over the Llanos, the Orinoco Delta sea breeze generates the C1 core as the advected cool maritime air flows downslope at the western limits of the Guanipa Mesa. Although density currents are known to spawn bores or solitary waves as they propagate in stably stratified environments, the size and propagation speed of the overall gravity current inhibit such behavior.

As the merged density current and large-scale flow move along the Orinoco River basin, the interaction with geographic points in the surrounding topography create point wakes at three fixed locations: the Guiana Highlands, Eastern Cordillera, and Macarena mountain range. Supercritical-channel-flow theory explains the expansion fans generated by these point wakes and properly predicts their final wind speeds and PBL heights. Such expansion fans give origin to the C2–C4 core regions.

A momentum balance budget performed for each one of the core locations shows that the diurnal variation of turbulent diffusivity decelerates (day) and accelerates (night) the horizontal winds across the domain, triggering the inertial oscillation mechanism and causing the clockwise rotation of the wind. However, opposite to what happens in higher latitudes, the role of the diurnal variation of turbulent diffusivity in the OLLJ acceleration is secondary, given that the maxima wind speeds as the result of combined geostrophic and ageostrophic winds occur in only two of the four cores. The cores closer to the equator (C3–C4) are driven by ageostrophic effects

on the wind due to the large imbalance in the geostrophic wind as the Coriolis parameter f becomes small.

Although dynamical downscaling and the momentum equation decomposition improve the current OLLJ characterization and understanding about the dynamics behind its formation, additional contributions are yet to be resolved. For instance, what is the role of latent heat release over the Amazon forest on the strength of the LLJ? Would some form of the OLLJ still occur in the partial or complete absence of terrain? What is the overall contribution of the radiative heating to its formation? Does the OLLJ vary according to warm or cold ENSO phases? Answers to these questions will improve our understanding of the OLLJ and will foster a better grasp of the influence of the OLLJ on wind energy, aviation safety, fire weather, oil-extraction pollutants transport, and public health, among others.

Acknowledgments

The research was supported by the Colombian Air Force and Colfuturo – Colciencias fellowships. Simulations were performed using the Advanced Cyberinfrastructure (ACI) of Penn State's Institute for Cyberscience, which can be found at: https://doi.org/10.26208/jaky-kq22. The assistance of Chuck Pavloski and the rest of the ICS staff was indispensable. The GFS Analysis were provided from the website of Research Data Archive (from http://rda.ucar.edu/datasets/ds335.0/). We are also grateful for the critiques provided by the anonymous reviewers; whose comments and suggestions greatly improved the article. Furthermore, the lead author thanks Prof. Andrew Carleton for a thorough review of an earlier version of this work while serving on the lead author's dissertation committee. The lead author is an active member of the Colombian Air Force.

Appendix A

Supercritical-Channel-Flow Hydraulic Theory Uncertainty Estimation

The uncertainties in the calculations presented in section 3.3 and Table 2 are estimated as follows. The total uncertainty, δq ,of a function $q(x,\ldots,z)$ for which the uncertainties in $x,\ldots,z$ are $\delta x,\ldots,\delta z$, respectively, is estimated via Taylor (1997) as

$$\delta q = \sqrt{\left(\frac{\partial q}{\partial x}\delta x\right)^2 + \ldots + \left(\frac{\partial q}{\partial z}\delta z\right)^2} \qquad \text{(A1)}$$

In the supercritical-channel-flow cases analyzed in Section 3, upstream wind speed and PBL height, lower-troposphere static stability, and the angular change in the flow direction due to the bending boundary (Figs. 6, 8, 10, and 12) are obtained from visual inspection of the respective fields and determine Fr and $d\theta$, along with their corresponding uncertainties. For instance, using Eq. (A1), the total uncertainty in the Froude Number (δFr ¿ upstream of the Guiana Highland expansion fan is given by

$$\delta Fr = \sqrt{\left(\frac{\partial Fr}{\partial U}\delta U\right)^2 + \left(\frac{\partial Fr}{\partial g'}\delta g'\right)^2 + \left(\frac{\partial Fr}{\partial h}\delta h\right)^2}$$

(A2)

554 $$\delta Fr = 0.22$$

555 so that $Fr = 1.32 \pm 0.22$.

556 The measured values and uncertainties of Fr and $d\theta$ propagate through the subsequent
557 calculations in Eqs. (4)–(7). The total uncertainty for every new variable is obtained using Eq.
558 (A1), with the exception of $\delta\beta$ in Eq. (4), where β is a function ofFr only, for which a simpler
559 formula can be used:

560 $$\delta\beta = \left|\frac{d\beta}{dFr}\right| \delta Fr \quad \text{(A3)}$$

561 Table 2 summarizes the predicted final wind speeds, PBL heights, and the corresponding
562 uncertainties for each expansion fan.

563

564 **References**

565 Amador, J. A. (2008). The Intra-Americas Sea low-level jet: Overview and future research.
566 *Annals of the New York Academy of Sciences*, *1146*(1), 153–188.
567 https://doi.org/10.1196/annals.1446.012

568 Balmez, M., & Ştefan, S. (2014). On the formation mechanism of low-level jet over Bucharest's
569 airports. *Atmosphere Physics*, *59*(Figure 1), 792–807.

570 Blackadar, A. K. (1957). Boundary layer wind maxima and their significance for the growth of
571 nocturnal inversions. *Bulletin of the American Meteorological Society*, *38*, 283–290.

572 Bonner, W. D. (1963). Thunderstorms and the low-level jets, 19–33.

573 Bonner, W. D. (1968). Climatology of the Low Level Jet. *Monthly Weather Review*, *96*(12),
574 833–850. https://doi.org/10.1175/1520-0493(1968)096<0833:COTLLJ>2.0.CO;2

575 Bonner, W. D., & Paegle, J. (1970). Diurnal variations in boundary layer winds over the south-
576 central united states in summer. *Monthly Weather Review*, *98*(10), 735–744. https://doi.org/
577 10.1175/1520-0493(1970)098<0735:DVIBLW>2.3.CO;2

578 Chen, G. T.-J., & Hsu, Y.-S. (1997). Composite structure of a Low-Level Jet over Southern
579 China observed during the TAMEX period. *Journal of the Meteorological Society of Japan*,
580 *75*(6), 1003–1018.

581 Chen, R., & Tomassini, L. (2015). The Role of Moisture in Summertime Low-Level Jet
582 Formation and Associated Rainfall over the East Asian Monsoon Region. *Journal of the*
583 *Atmospheric Sciences*, *72*(10), 3871–3890. https://doi.org/10.1175/JAS-D-15-0064.1

584 Clarke, R. H., Smith, R. K., & Reid, D. G. (1981). The Morning Glory of the Gulf of
585 Carpentaria: An Atmospheric Undular Bore. *Monthly Weather Review*, *109*(8), 1726–1750.
586 https://doi.org/10.1175/1520-0493(1981)109<1726:TMGOTG>2.0.CO;2

587 Coleman, T. A., Knupp, K. R., & Herzmann, D. E. (2010). An undular bore and gravity waves
588 illustrated by dramatic time-lapse photography. *Journal of Atmospheric and Oceanic*
589 *Technology*, 1355–1361. https://doi.org/10.1175/2010JTECHA1472.1

590 Cook, K. H., & Vizy, E. K. (2010). Hydrodynamics of the Caribbean low-level jet and its

relationship to precipitation. *Journal of Climate*, *23*(6), 1477–1494. https://doi.org/10.1175/2009JCLI3210.1

Douglas, M., Murillo, J., & Mejia, J. (2005). Conducting short duration field programs to evaluate sounding site representativeness and potential climate monitoring biases. Examining the low-level jet over the Venezuelan llanos during the 2005 dry season. In *15th Conference on Applied Climatology*. Savannah, GA. Retrieved from http://www.nssl.noaa.gov/projects/pacs

Doyle, J. D., & Warner, T. T. (1993). A three-dimensional numerical investigation of a Carolina Coastal Low-Level Jet during GALE IOP 2. *Monthly Weather Review*, *121*(4), 1030–1047. https://doi.org/10.1175/1520-0493(1993)121<1030:ATDNIO>2.0.CO;2

Du, Y., & Rotunno, R. (2014). A Simple Analytical Model of the Nocturnal Low-Level Jet over the Great Plains of the United States. *Journal of the Atmospheric Sciences*, *71*(10), 3674–3683. https://doi.org/10.1175/JAS-D-14-0060.1

Du, Y., Zhang, Q., Chen, Y. L., Zhao, Y., & Wang, X. (2014). Numerical simulations of spatial distributions and diurnal variations of low-level jets in China during early summer. *Journal of Climate*, *27*(15), 5747–5767. https://doi.org/10.1175/JCLI-D-13-00571.1

Du, Y., Rotunno, R., & Zhang, Q. (2015). Analysis of WRF-Simulated Diurnal Boundary Layer Winds in Eastern China Using a Simple 1D Model. *Journal of the Atmospheric Sciences*, *72*(2), 714–727. https://doi.org/10.1175/JAS-D-14-0186.1

Du, Y., Chen, Y.-L., & Zhang, Q. (2015). Numerical Simulations of the Boundary Layer Jet off the Southeastern Coast of China. *Monthly Weather Review*, *143*(4), 1212–1231. https://doi.org/10.1175/MWR-D-14-00348.1

Fedorovich, E., Gibbs, J. A., & Shapiro, A. (2017). Numerical Study of Nocturnal Low-Level Jets over Gently Sloping Terrain. *Journal of the Atmospheric Sciences*, *74*(9), 2813–2834. https://doi.org/10.1175/JAS-D-17-0013.1

Findlater, J. (1969). A major low level air current near the Indian Ocean during the northern summer. *Quarterly Journal of the Royal Meteorological Society*, *95*, 362–380.

Foghin-Pillin, S. (2016). Evidencias de la penetración de brisas de mar en la depresión del río Unare y Llanos de Anzoátegui. *Revista de Investigación*, *40*(87), 39–62.

Giannakopoulou, E. M., & Toumi, R. (2012). The Persian Gulf summertime low-level jet over sloping terrain. *Quarterly Journal of the Royal Meteorological Society*, *138*(662), 145–157. https://doi.org/10.1002/qj.901

Gilford, M. T., Bonam, R. C., Martens, D. L., Myles, G., & Vojtesak, M. J. (1992). *South America South of the Amazon River – A Climatological Study*. Scott Air Force Base, Illinois, USA: USAF Environmental Technical Applications Center.

Goler, R. A., & Reeder, M. J. (2004). The Generation of the Morning Glory, 1360–1376.

Haase, S. P., & Smith, R. K. (1989). The numerical simulation of atmospheric gravity currents. Part II: Environments with stable layers. *Geophys. Astrophys. Fluid Dynamics*, *46*, 35–51.

Hart, J. E. (1977). On the theory of the East African Low Level Jet Stream. *Pure and Applied Geophysics PAGEOPH*, *115*(5–6), 1263–1282. https://doi.org/10.1007/BF00874409

He, M.-Y., Liu, H. B., Wang, B., & Zhang, D. L. (2016). A modeling study of a low-level jet along the Yun-Gui Plateau in South China. *Journal of Applied Meteorology and Climatology*, *55*(1), 41–60. https://doi.org/10.1175/JAMC-D-15-0067.1

Hidalgo, H. G., Durán-Quesada, A. M., Amador, J. A., & Alfaro, E. J. (2015). The caribbean low-level jet, the inter-tropical convergence zone and precipitation patterns in the intra-Americas Sea: A proposed dynamical mechanism. *Geografiska Annaler, Series A: Physical Geography*, *97*(1), 41–59. https://doi.org/10.1111/geoa.12085

Holton, J. R. (1967). The diurnal boundary layer wind oscillation above sloping terrain. *Tellus*, *19*(2), 199–205. https://doi.org/10.3402/tellusa.v19i2.9766

Jiménez-Sánchez, G., Markowski, P., Jewtoukoff, V., Young, G., & Stensrud, D. J. (2019). The Orinoco Low-Level Jet: An Investigation of Its Characteristics and Evolution Using the WRF Model. *Journal of Geophysical Research: Atmospheres*, *124*(20), 10696–10711. https://doi.org/10.1029/2019JD030934

Juliano, T. W., Parish, T. R., Rahn, D. A., & Leon, D. C. (2017). An atmospheric hydraulic jump in the Santa Barbara Channel. *Journal of Applied Meteorology and Climatology*, 2981–2999. https://doi.org/10.1175/JAMC-D-16-0396.1

Koch, S. E., & Clark, W. L. (1999). A Nonclassical Cold Front Observed during COPS-91: Frontal Structure and the Process of Severe Storm Initiation. *Journal of the Atmospheric Sciences*, *56*(16), 2862–2890. https://doi.org/10.1175/1520-0469(1999)056<2862:ANCFOD>2.0.CO;2

Koch, S. E., Pagowski, M., Wilson, J. W., Fabry, F., Flamant, C., Feltz, W., et al. (2005). The Structure and Dynamics of Atmospheric Bores and Solitons and Modeling Experiments during IHOP. In *11th Conference on Mesoscale Processes and the 32nd Conference on Radar Meteorology* (p. 14).

Krishnamurthy, L., Vecchi, G. A., Msadek, R., Wittenberg, A., Delworth, T. L., & Zeng, F. (2015). The seasonality of the great plains low-level Jet and ENSO relationship. *Journal of Climate*, *28*(11), 4525–4544. https://doi.org/10.1175/JCLI-D-14-00590.1

Labar, R. J., Douglas, M., Murillo, J., & Mejia, J. F. (2005). The Llanos low-level jet and its association with Venezuelan convective precipitation. *Weather*, *98926*(August), 1–21.

Liu, M., Westphal, D. L., Holt, T. R., & Xu, Q. (2000). Numerical Simulation of a Low-Level Jet over Complex Terrain in Southern Iran. *Monthly Weather Review*, *128*(5), 1309–1327. https://doi.org/10.1175/1520-0493(2000)128<1309:NSOALL>2.0.CO;2

Maldonado, T., Rutgersson, A., Amador, J., Alfaro, E., & Claremar, B. (2016). Variability of the Caribbean low-level jet during boreal winter: Large-scale forcings. *International Journal of Climatology*, *36*(4), 1954–1969. https://doi.org/10.1002/joc.4472

Maldonado, T., Rutgersson, A., Caballero, R., Pausata, F. S. R., Alfaro, E., & Amador, J. (2017). The role of the meridional sea surface temperature gradient in controlling the Caribbean low-level jet. *Journal of Geophysical Research: Atmospheres*, *122*(11), 5903–5916. https://doi.org/10.1002/2016JD026025

Marengo, J. A., Soares, W. R., Saulo, C., & Nicolini, M. (2004). Climatology of the low-level jet east of the Andes as derived from the NCEP-NCAR reanalyses: Characteristics and

672 temporal variability. *Journal of Climate*, *17*(12), 2261–2280. https://doi.org/10.1175/1520-
673 0442(2004)017<2261:COTLJE>2.0.CO;2

674 Moisseeva, N., & Steyn, D. G. (2014). Dynamical analysis of sea-breeze hodograph rotation in
675 Sardinia. *Atmospheric Chemistry and Physics*, *14*(24), 13471–13481.
676 https://doi.org/10.5194/acp-14-13471-2014; 10.5194/acp-14-13471-2014-supplement.

677 Montini, T. L., Jones, C., & Carvalho, L. M. V. (2019). The South American Low-Level Jet: A
678 New Climatology, Variability, and Changes. *Journal of Geophysical Research:*
679 *Atmospheres*, *124*(3). https://doi.org/10.1029/2018JD029634

680 Montoya, G. J., Pelkowski, J., & Eslava, J. (2001). Sobre los alisios del nordeste y la existencia
681 de una corriente en el piedemonte oriental Andino. *Rev. Acad. Colomb. Cienc*, *25*(96), 363–
682 370. https://doi.org/0370-3908

683 Muñoz, E., Busalacchi, A. J., Nigam, S., & Ruiz-Barradas, A. (2008). Winter and summer
684 structure of the Caribbean low-level jet. *Journal of Climate*, *21*(6), 1260–1276.
685 https://doi.org/10.1175/2007JCLI1855.1

686 Do Nascimento, M. G., Herdies, D. L., & De Souza, D. O. (2016). The south American water
687 balance: The influence of low-level jets. *Journal of Climate*, *29*(4), 1429–1449.
688 https://doi.org/10.1175/JCLI-D-15-0065.1

689 Nicholson, S. (2016). The Turkana low-level jet: Mean climatology and association with
690 regional aridity. *International Journal of Climatology*, *36*(6), 2598–2614.
691 https://doi.org/10.1002/joc.4515

692 Outten, S. D., Renfrew, I. A., & Petersen, G. N. (2009). An easterly tip jet off Cape Farewell,
693 Greenland. II: Simulations and dynamics. *Quarterly Journal of the Royal Meteorological*
694 *Society*, *135*, 1934–1949. https://doi.org/10.1002/qj.531

695 Parish, T. R. (2017). On the Forcing of the Summertime Great Plains Low-Level Jet. *Journal of*
696 *the Atmospheric Sciences*, *74*(12), 3937–3953. https://doi.org/10.1175/JAS-D-17-0059.1

697 Patricola, C. M., & Chang, P. (2017). Structure and dynamics of the Benguela low-level coastal
698 jet. *Climate Dynamics*, *49*(7–8), 2765–2788. https://doi.org/10.1007/s00382-016-3479-7

699 Poveda, G., & Mesa, O. (1999). La Corriente de chorro superficial del oeste ("del Chocó") y
700 otras dos corrientes de chorro en Colombia: Climatología y Variabilidad durante las fases
701 del ENSO. *Rev. Acad. Colomb. Cienc*, *23*(89), 517–528.

702 Poveda, G., & Mesa, O. J. (2000). On the Existence of Lloro (the Rainiest Locality on Earth):
703 Enhanced Ocean-Land-Atmosphere Interaction by a Low- Level Jet. *Geophysical Research*
704 *Letters*, *27*(11), 1675–1678.

705 Poveda, G., Jaramillo, L., & Vallejo, L. F. (2014). Seasonal precipitation patterns along
706 pathways of South American low-level jets and aerial rivers. *Water Resources Research*,
707 *50*(1), 98–118. https://doi.org/10.1002/2013WR014087

708 Prabha, T. V., Goswami, B. N., Murthy, B. S., & Kulkarni, J. R. (2011). Nocturnal low-level jet
709 and "atmospheric streams" over the rain shadow region of indian western ghats. *Quarterly*
710 *Journal of the Royal Meteorological Society*, *137*(658), 1273–1287. https://doi.org/10.1002/
711 qj.818

Reeder, M. J., Smith, R. K., Taylor, J. R., Low, D. J., Arnup, S. J., Muir, L., & Thomsen, G. (2013). Diurnally forced convergence lines in the australian tropics. *Quarterly Journal of the Royal Meteorological Society*, *139*(674), 1283–1297. https://doi.org/10.1002/qj.2021

Rife, D. L., Pinto, J. O., Monaghan, A. J., Davis, C. A., & Hannan, J. R. (2010). Global distribution and characteristics of diurnally varying low-level jets. *Journal of Climate*, *23*(19), 5041–5064. https://doi.org/10.1175/2010JCLI3514.1

Rogerson, A. M. (1999). Transcritical Flows in the Coastal Marine Atmospheric Boundary Layer*. *Journal of the Atmospheric Sciences*, *56*(16), 2761–2779. https://doi.org/10.1175/1520-0469(1999)056<2761:TFITCM>2.0.CO;2

Rojas, G. M. (2008). *Low level jets in the tropical americas*. Colorado State University.

Rueda, C. (2015). *Caracterización de la corriente en chorro de bajo nivel de los llanos orientales colombianos (Characterization of the low-level jet over the Colombian Eastern llanos)*. Universidad Nacional de Colombia, Bogotá, Colombia.

Rueda, O., & Poveda, G. (2006). Variabilidad espacial y temporal del chorro del "Chocó" y su efecto en la hidroclimatología de la región del pacífico colombiano. *Meteorol. Col*, (501), 132–145.

Samelson, R. M. (1992). Supercritical Marine-Layer Flow along a Smoothly Varying Coastline. *Journal of the Atmospheric Sciences*, *49*, 1571–1584. https://doi.org/10.1175/1520-0469(1992)049<1571:SMLFAA>2.0.CO;2

Shapiro, A., Fedorovich, E., & Rahimi, S. (2016). A Unified Theory for the Great Plains Nocturnal Low-Level Jet. *Journal of the Atmospheric Sciences*, *73*(8), 3037–3057. https://doi.org/10.1175/JAS-D-15-0307.1

Silva, G. A. M., Ambrizzi, T., & Marengo, J. A. (2009). Observational evidences on the modulation of the South American Low Level Jet east of the Andes according the ENSO variability. *Ann. Geophys*, *27*, 645–657. https://doi.org/10.5194/angeo-27-645-2009

Simpson, J. E. (1987). *Gravity currents: in the environment and the laboratory*. Chichester, West Susex, England: Ellies Horwood Limited.

Simpson, J. E. (1994). *Sea breeze and local winds*. Cambridge: Cambridge University Press.

Skamarock, W. C., & Klemp, J. B. (2008). A time-split nonhydrostatic atmospheric model for weather research and forecasting applications. *Journal of Computational Physics*, *227*(7), 3465–3485. https://doi.org/10.1016/j.jcp.2007.01.037

Smith, R. K., Roff, G., & Crook, N. (1982). The Morning Glory: An extraordinary atmospheric undular bore. *Quarterly Journal of the Royal Meteorological Society*, *8*, 937–956. https://doi.org/10.1002/qj.49710845813

Soares, P. M. M., Cardoso, R. M., Semedo, Á., Chinita, M. J., & Ranjha, R. (2014). Climatology of the Iberia coastal low-level wind jet: Weather research forecasting model high-resolution results. *Tellus, Series A: Dynamic Meteorology and Oceanography*, *66*(1), 1–19. https://doi.org/10.3402/tellusa.v66.22377

Söderberg, S., & Tjernström, M. (2001). Supercritical channel flow in the coastal atmospheric boundary layer: Idealized numerical simulations. *Journal of Geophysical Research:*

752 *Atmospheres*, *106*(D16), 17811–17829. https://doi.org/10.1029/2001JD900195

753 Song, J., Liao, K. E., Coulter, R. L., & Lesht, B. M. (2005). Climatology of the Low-Level Jet at
754 the Southern Great Plains Atmospheric Boundary Layer Experiments Site. *Journal of*
755 *Applied Meteorology*, *44*(1968), 1593–1606. https://doi.org/10.1175/JAM2294.1

756 Squitieri, B. J. (2014). *WRF forecast skill of the Great Plains low level jet and its correlation to*
757 *forecast skill of mesoscale convective system precipitation*. Iowa State University.

758 Stensrud, D. J. (1996). Importance of low-level jets to climate: A review. *Journal of Climate*,
759 *9*(8), 1698–1711. https://doi.org/10.1175/1520-0442(1996)009<1698:IOLLJT>2.0.CO;2

760 Stull, R. (2015a). Atmospheric Boundary Layer. In *Practical Meteorology: An algebra-based*
761 *survey of atmospheric science* (pp. 687–722). Vancouver, BC, Canada: University of British
762 Columbia.

763 Stull, R. (2015b). Regional Winds. In *Practical Meteorology: An algebra-based survey of*
764 *atmospheric science* (pp. 645–686). Vancouver, BC, Canada: University of British
765 Columbia.

766 Taylor, J. R. (1997). *An introduction to error analysis: The study of uncertainties in physical*
767 *measurements* (2nd Ed.). Sausalito, California: University Science Books.

768 Torrealba, E. R., & Amador, J. A. (2010). La corriente en chorro de bajo nivel sobre los Llanos
769 Venezolanos de Sur América. *Revista de Climatología*, *10*(July), 1–10.

770 Tripaldi, A., & Zárate, M. A. (2016). A review of Late Quaternary inland dune systems of South
771 America east of the Andes. *Quaternary International*, *410*, 96–110. https://doi.org/10.1016/
772 j.quaint.2014.06.069

773 Tsai, V. C., Kanamori, H., & Artru, J. (2004). The morning glory wave of southern California. *J.*
774 *Geophys. Res*, *109*(October 2001), 1–11. https://doi.org/10.1029/2003JB002596

775 Vera, C., Baez, J., Douglas, M., Emmanuel, C. B., Marengo, J., Meitin, J., et al. (2006). The
776 South American low-level jet experiment. *Bulletin of the American Meteorological Society*,
777 *87*(1), 63–77. https://doi.org/10.1175/BAMS-87-1-63

778 Vernekar, A. D., Kirtman, B. P., & Fennessy, M. J. (2003). Low-level jets and their effects on
779 the South American summer climate as simulated by the NCEP Eta Model. *Journal of*
780 *Climate*, *16*(2), 297–311. https://doi.org/10.1175/1520-
781 0442(2003)016<0297:LLJATE>2.0.CO;2

782 Virji, H. (1981). A Preliminary Study of Summertime Tropospheric Circulation Patterns over
783 South America Estimated from Cloud Winds. *Mon Weather Rev*, *109*(3), 599–610.
784 https://doi.org/10.1175/1520-0493(1981)109<0599:APSOST>2.0.CO;2

785 Wang, H., Fu, R., Schemm, J. K., Tang, W., & Liu, W. T. (2008). Predictability of South
786 American low-level jet using QuikSCAT ocean surface wind. *International Journal of*
787 *Remote Sensing*, *29*(21), 6117–6127. https://doi.org/10.1080/01431160802175512

788 Watson, C. D., & Lane, T. P. (2016). A Case of an Undular Bore and Prefrontal Precipitation in
789 the Australian Alps, (2008), 2623–2644. https://doi.org/10.1175/MWR-D-15-0355.1

790 Weaver, S. J., & Nigam, S. (2008). Variability of the great plains low-level jet: Large-scale
791 circulation context and hydroclimate impacts. *Journal of Climate*, *21*(7), 1532–1551.

https://doi.org/10.1175/2007JCLI1586.1

Wei, W., Wu, B. G., Ye, X. X., Wang, H. X., & Zhang, H. S. (2013). Characteristics and Mechanisms of Low-Level Jets in the Yangtze River Delta of China. *Boundary-Layer Meteorology*, *149*(3), 403–424. https://doi.org/10.1007/s10546-013-9852-8

Wexler, H. (1961). A Boundary Layer Interpretation of the Low-level Jet. *Tellus*, *13*(3), 368–378. https://doi.org/10.1111/j.2153-3490.1961.tb00098.x

Whiteman, C. D., Bian, X., & Zhong, S. (1997). Low-Level Jet Climatology from Enhanced Rawinsonde Observations at a Site in the Southern Great Plains, 1363–1376.

Whyte, F. S., Taylor, M. A., Stephenson, T. S., & Campbell, J. D. (2008). Features of the Caribbean low level jet. *International Journal of Climatology*, *28*(1), 119–128. https://doi.org/10.1002/joc.1510

Van de Wiel, B. J. H., Moene, A. F., Steeneveld, G. J., Baas, P., Bosveld, F. C., & Holtslag, A. A. M. (2010). A Conceptual View on Inertial Oscillations and Nocturnal Low-Level Jets. *Journal of the Atmospheric Sciences*, *67*(8), 2679–2689. https://doi.org/10.1175/2010JAS3289.1

Winant, C. D., Dorman, C. E., Friehe, C. A., & Beardsley, R. C. (1988). The marine layer off Northern California: an example of supercritical channel flow. *Journal Of The Atmospheric Sciences*, *45*(23), 3588–3605. https://doi.org/10.1175/1520-0469(1988)045<3588:TMLONC>2.0.CO;2

Wu, Y., & Raman, S. (1993). The Great Plains Low-Level Jet (LLJ) During the Atmospheric Radiation Measurement (ARM) Intensive Observation Period (IOP) -4 and Simulations of Land Use Pattern Effect on the LLJ Simulations of Land Use Pattern Effect on the LLJ Model Description (pp. 367–371).

Young, G., & Winstead, N. (2005). Meteorological phenomena in high resolution SAR wind imagery. In *High resolution wind monitoring with wide swath SAR: A user's guide* (pp. 13–32). Washington DC, USA: National Oceanic and Atmospheric Administration.

Zhao, P., Sun, J., & Zhou, X. (2003). Mechanism of formation of low level jets in the South China Sea during spring and summer of 1998. *Chinese Science Bulletin*, *48*(12), 1265–1270.